



Origin and Evolution of Short-period Comets

David Nesvorný¹, David Vokrouhlický², Luke Dones¹, Harold F. Levison¹, Nathan Kaib³, and Alessandro Morbidelli⁴

¹Department of Space Studies, Southwest Research Institute, 1050 Walnut St., Suite 300, Boulder, CO 80302, USA

²Institute of Astronomy, Charles University, V Holešovičkách 2, CZ-18000 Prague 8, Czech Republic

³H.L. Dodge Department of Physics and Astronomy, University of Oklahoma, Norman, OK 73019, USA

⁴Département Cassiopée, University of Nice, CNRS, Observatoire de la Côte d'Azur, Nice, F-06304, France

Received 2017 April 25; revised 2017 June 22; accepted 2017 June 28; published 2017 August 9

Abstract

Comets are icy objects that orbitally evolve from the trans-Neptunian region into the inner solar system, where they are heated by solar radiation and become active due to the sublimation of water ice. Here we perform simulations in which cometary reservoirs are formed in the early solar system and evolved over 4.5 Gyr. The gravitational effects of Planet 9 (P9) are included in some simulations. Different models are considered for comets to be active, including a simple assumption that comets remain active for $N_p(q)$ perihelion passages with perihelion distance $q < 2.5$ au. The orbital distribution and number of active comets produced in our model is compared to observations. The orbital distribution of ecliptic comets (ECs) is well reproduced in models with $N_p(2.5) \simeq 500$ and without P9. With P9, the inclination distribution of model ECs is wider than the observed one. We find that the known Halley-type comets (HTCs) have a nearly isotropic inclination distribution. The HTCs appear to be an extension of the population of returning Oort-cloud comets (OCCs) to shorter orbital periods. The inclination distribution of model HTCs becomes broader with increasing N_p , but the existing data are not good enough to constrain N_p from orbital fits. $N_p(2.5) > 1000$ is required to obtain a steady-state population of large active HTCs that is consistent with observations. To fit the ratio of the returning-to-new OCCs, by contrast, our model implies that $N_p(2.5) \lesssim 10$, possibly because the detected long-period comets are smaller and much easier to disrupt than observed HTCs.

Key words: comets: general

1. Introduction

Comets are icy objects that reach the inner solar system after leaving distant reservoirs beyond Neptune and dynamically evolving onto elongated orbits with very low perihelion distances (see Dones et al. 2015 for a review). Their activity, manifesting itself by the presence of a dust/gas coma and characteristic tail, is driven by solar heating and sublimation of water ice. Comets are short lived, implying that they must be resupplied from external reservoirs (Fernández 1980; Duncan et al. 1988). The goal of this work is to model the formation of cometary reservoirs early in the solar system history, follow their evolution to the present time, and see how observations of comets can be used to constrain the orbital structure of trans-Neptunian populations. Our main focus is the short-period comets (SPCs), because the population of comets with short orbital periods ($P < 200$ yr) is relatively well characterized from observations and allows us to meaningfully constrain the model. We aim at a better understanding of the origin and dynamical/physical evolution of SPCs.

Levison & Duncan (1997, hereafter LD97) considered the origin and evolution of ecliptic comets (ECs; see Section 2 for a definition and their relationship to the Jupiter-family comets, JFCs). The Kuiper Belt at 30–50 au was assumed in LD97 to be the main source of ECs. They showed that small Kuiper Belt objects (KBOs) reaching a Neptune-crossing orbit can be slingshot, by encounters with different planets, to very low perihelion distances ($q < 2.5$ au), at which point they are expected to become active and visible. The new ECs, reaching $q < 2.5$ au for the first time, have a narrow inclination distribution in the LD97 model, because their orbits were assumed to start with low inclinations ($i < 5^\circ$) in the Kuiper Belt, and the inclinations stayed low during the orbital transfer.

LD97 pointed out that the inclination distribution of ECs becomes wider over time due to scattering encounters with Jupiter. The best fit to the observed inclination distribution of ECs was obtained in LD97 when it was assumed that ECs remain active for $\simeq 12,000$ years after first reaching $q < 2.5$ au.

The escape of bodies from the classical Kuiper Belt at 30–50 au (hereafter classical KB) is driven by slow chaotic processes in various orbital resonances with Neptune. Because these processes affect only part of the belt, with most orbits in the belt being stable, questions arise about the overall efficiency of comet delivery from the classical KB. Duncan & Levison (1997), concurrently with the discovery of the first Scattered Disk Object (SDO; (15874) 1996 TL66, Luu et al. 1997), suggested that the scattered disk should be a more prolific source of ECs than the classical KB (see Gladman et al. 2008 for a formal definition of these dynamical classes). This is because SDOs can approach Neptune during their perihelion passages and be scattered by Neptune to orbits with shorter orbital periods. The scattered disk should thus produce more ECs than the unstable part of the classical KB.

The inclination distribution of SDOs is wider than the one used as the source of ECs in LD97. This is because the scattered disk is in contact with Neptune, and the orbital inclinations of SDOs increase over time by scattering encounters with Neptune. In fact, the inclination distribution of SDOs (median $i \simeq 25^\circ$; Nesvorný et al. 2016) is much broader than that of ECs (median $i \simeq 13^\circ$; Section 2). This raises the question whether the scattered disk can produce the narrow inclination distribution of ECs (Rickman et al. 2017). Di Sisto et al. (2009) tested this issue but assumed that SDOs have lower inclinations (Di Sisto & Brunini 2007 median $i \simeq 15^\circ$; their Figure 3) than they have in reality (Kaib & Sheppard 2016; Nesvorný et al. 2016).

The Halley-type comets (HTCs) have longer orbital periods and larger inclinations than do most ECs. The HTCs population is not well characterized from the existing observations, because the observational biases for long orbital periods are more severe than for ECs (see Section 2). Levison et al. (2001) studied the origin and evolution of HTCs. They suggested that HTCs evolve into the inner solar system from an inner, presumably flattened part of the Oort cloud. This theory was motivated by the inclination distribution of HTCs, which at the time of the Levison et al. work was thought to be flattened with a median of $\simeq 45^\circ$. Later on, Levison et al. (2006) considered the scattered disk to be the main source of HTCs and showed that some SDOs can evolve into the Oort cloud and back, thus providing an anisotropic source of HTCs. Back in 2006, the median orbital inclination of HTCs was thought to be $\simeq 55^\circ$, somewhat larger than in 2001, but still clearly anisotropic. This turns out to be part of a historical trend (Wang & Brasser 2014 and Section 2).

Our understanding of the origin and evolution of comets is incomplete in part because the presumed source populations of trans-Neptunian objects with cometary sizes ($\sim 1\text{--}10$ km) are not well characterized from observations. It is therefore difficult to establish whether there are enough small objects in any trans-Neptunian reservoir to provide the source of comets (e.g., Volk & Malhotra 2008). Turning this argument around, previous studies typically assumed that a specific type of comet comes from a specific reservoir (e.g., ECs from the scattered disk), reconstructed that reservoir from observations and theoretical considerations, and modeled comet delivery from the reservoir to infer how many comet-size objects currently need to be in the reservoir to explain the observed population of comets.

For example, Brasser & Morbidelli (2013, hereafter BM13) found that the scattered disk needs to contain $\sim 2 \times 10^9$ bodies with diameter $D > 2.3$ km to provide an adequate source of ECs, and the Oort cloud needs to have $\sim 4 \times 10^{10}$ to $\sim 10^{11}$ bodies with $D > 2.3$ km to explain the flux of new Oort cloud comets (OCCs). Rickman et al. (2017) suggested that there are $\sim 10^9$ SDOs with $D > 2$ km from the modeling of ECs. Levison et al. (2006), on the other hand, required there to be $\sim 3 \times 10^9$ SDOs with $D > 10$ km to produce the observed population of HTCs, assuming no physical evolution (more SDOs would be needed if they accounted for the physical disruption/fading of HTCs).

Although some of these estimates may appear to be high, it is not obvious whether they are implausibly high, because we just do not know from observations how many small objects there are in the distant regions. Another approach to this problem, which we pursue here, is to perform end-to-end simulations in which cometary reservoirs are produced in the early solar system and evolved over 4.5 Gyr (see also BM13). The number of comets produced in the model at $t = 4.5$ Gyr can be inferred from the number of comets in the original trans-planetary disk, which in turn can be calibrated from the number of Jupiter Trojans (Nesvorný & Vokrouhlický 2016, hereafter NV16). This is because the Trojan implantation efficiency from the original disk is well-determined (Nesvorný et al. 2013; see also Morbidelli et al. 2005) and because the size distribution of Trojans is not well defined from observations (e.g., Wong & Brown 2015, Yoshida & Terai 2017). If the calibration works, the model should match the observed number of comets, and

the number of comet-sized objects in the distant reservoirs can be inferred from it (Section 4.7).

This approach, to be reliable, requires that we have a good model for the early evolution of the solar system. Here we use the model developed in Nesvorný & Morbidelli (2012; hereafter NM12), which was inspired by many previous studies (e.g., Tsiganis et al. 2005; Morbidelli et al. 2007). NM12 performed a large number of self-consistent simulations of early planetary migration/instability in an attempt to identify the initial configuration and dynamical evolution of planets that would lead to the solar system as we know it now. This includes the number and orbits of the outer planets and the survival of the terrestrial planets. The identified solutions were scrutinized against various constraints from small-body populations, such as the asteroid and Kuiper belts, Jupiter Trojans, and regular and irregular moons of the outer planets (see NV16 and references therein), showing the general applicability of the NM12 model to various problems. Here we use the NM12 model to study cometary populations.

In Section 2, we discuss the dynamical classification of SPCs, their orbital distribution, and physical properties. Our model is explained in Section 3. The results are reported in Section 4 and discussed in Section 5. We confirm the conclusion of previous studies that the scattered disk is the main source of ECs, and find that the Oort cloud is the main source of HTCs. Planet 9 (hereafter P9), hypothesized to exist on a wide orbit around the Sun (Trujillo & Sheppard 2014; Batygin & Brown 2016a), is included in some of our simulations (see Section 3) to test its influence on the structure of the trans-Neptunian region and comet delivery. We find that P9 would enhance the flux of HTCs by $\sim 30\%$. The inclination distribution of ECs can be matched in a straightforward manner in a model without P9, but when P9 is included, it acts to increase the inclination dispersion of SDOs. This propagates into the inclination distribution of ECs, which then appears to be too broad to match observations.

2. Properties of Known SPCs

SPCs are defined as bodies showing cometary activity and having short orbital periods ($P < 200$ yr).⁵ The period range is arbitrary, because there is nothing special about the boundary at the 200 yr period, and the orbital period distribution of known comets appears to continue smoothly across this boundary. With $P < 200$ yr, SPCs are guaranteed to have at least one perihelion passage in modern history, with many being observed multiple times. This contrasts with the situation for the long-period comets (LPCs; $P > 200$ yr), which can be detected only if their perihelion passage coincides with the present epoch.

Figure 1 shows the orbital distribution of known SPCs. We obtained these data from the JPL Small-Body Database Search Engine⁶ in January 2017. To reduce the influence of observational biases, we only show comets with *known* total (nucleus and coma) absolute magnitude, H_T . Comets that do not have H_T reported in the JPL database are discarded, because their detection circumstances are unclear. Paired bodies, such as fragments of the disrupted comet 73P/Schwassmann-Wachmann,

⁵ The main belt comets or “active” asteroids (Jewitt et al. 2015) are not considered here.

⁶ http://ssd.jpl.nasa.gov/sbdb_query.cgi

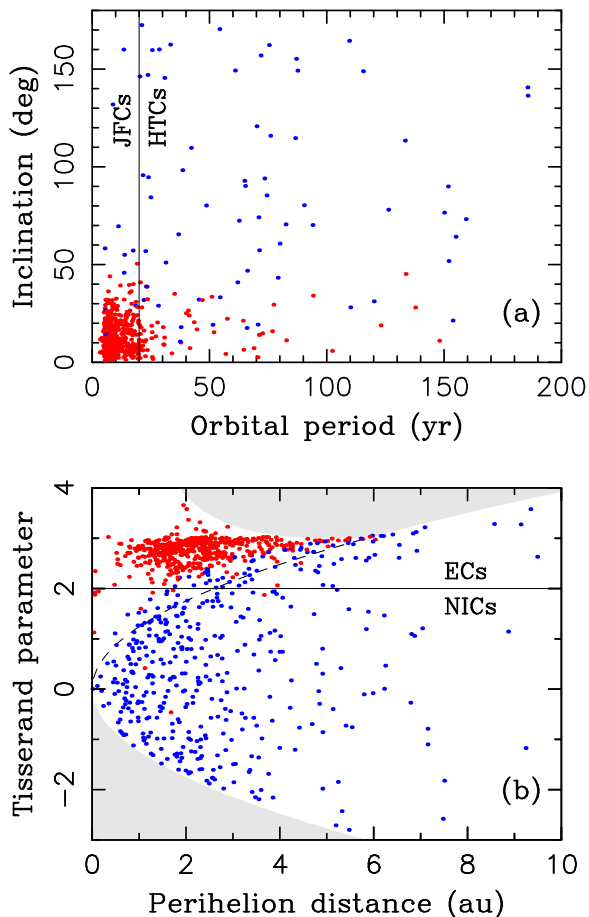


Figure 1. Orbital distribution of known SPCs. The thin lines show the division between JFCs and HTC regions (panel a; $P = 20$ yr), and between ECs and NICs (panel b; $T_J = 2$). The color indicates the relationship between different categories. In panel a, the red dots denote ECs with $T_J > 2$, and the blue dots denote NICs with $T_J < 2$. In panel b, the red dots denote JFCs with $P < 20$ yr, and the blue dots denote comets with $P > 20$ yr and $a < 10,000$ au. The gray areas in panel b cannot be reached by orbits. The dashed line in panel b is $T_J = 2\sqrt{2}q$, which is an approximate boundary of prograde orbits evolving from $a \gg a_J$ and $e \sim 1$.

were removed, leaving only one data point for each parent comet in Figure 1.

The orbital distribution of SPCs shows clear evidence for two populations, which are historically known as JFCs and HTCs. The JFC population is a tightly concentrated group in orbital space with short orbital periods and low inclinations. The HTC population is more dispersed in period–inclination space. These characteristics hint at different origins of JFCs and HTCs.

The distinction between JFCs and HTCs is blurred, at least to some degree, because the two populations partially overlap in orbital space. A traditional approach to the classification problem is to define JFCs as comets with $P < 20$ yr. This definition is motivated by the fact that the dense clump of comets in Figure 1(a) shows periods $5 \lesssim P \lesssim 20$ yr, which is similar to the orbital period of Jupiter ($P_J = 11.9$ yr). Another approach to this problem would be to use a criterion based on inclinations and define JFCs as comets with orbital inclinations lower than some threshold.

LD97 opted, instead, to use the Tisserand invariant of the circular restricted three-body problem (Tisserand 1889), which conveniently combines the comet’s orbital period (or, equivalently, the semimajor axis a) and inclination into a single expression. The

Tisserand parameter with respect to Jupiter, T_J , is defined as

$$T_J = \frac{a_J}{a} + 2\sqrt{(1 - e^2)\frac{a}{a_J}} \cos i, \quad (1)$$

where a_J is Jupiter’s semimajor axis, and e and i are the comet’s orbital eccentricity and inclination. Since Jupiter’s orbit is slightly eccentric, T_J is not strictly conserved and changes over time. Still, the evolution of T_J is much slower than the evolution of P , and T_J therefore represents a better classification parameter than P . It can be shown that $U/v_J = \sqrt{3 - T_J}$, where v_J is the orbital speed of Jupiter and U is the encounter speed between Jupiter (assumed to move on a strictly circular orbit) and a comet. Comets with T_J just below 3 can therefore have low-velocity encounters with Jupiter.

LD97 classified comets into two categories: (1) ECs with $2 < T_J < 3$, and (2) nearly isotropic comets (NICs) with $T_J < 2$. This classification is highlighted in Figure 1(b). Most JFCs ($P < 20$ yr) are ECs ($2 < T_J < 3$), and vice versa, and most HTCs ($20 < P < 200$ yr) are NICs ($T_J < 2$). The NIC category is broad, however, and includes LPCs as well. Orbits with $T_J > 3$ are generally not Jupiter crossing, and are therefore typically not classified as cometary (but note that those with T_J only slightly exceeding 3 can still cross the eccentric orbit of Jupiter). The Encke-type comets with $T_J > 3$ and aphelion distances $Q = a(1 + e) \lesssim 4.2$ au are not considered here.

There are two problematic regions of orbital space where the definitions based on the orbital period or Tisserand parameter have contradictory implications. First, several known comets with $P < 20$ yr have large orbital inclinations or even retrograde orbits (Figure 1(a)). They could be classified as JFCs and grouped with other low-inclination JFCs, which would be confusing, because they do not seem to be part of the JFC population. Instead, they appear to be a low-period extension of NICs. Second, the SPC population of low-inclination orbits extends from $P < 20$ yr to $P > 20$ yr, while the formal definition of JFCs based on the orbital period does not allow for that.⁷

Ideally, a good classification scheme should reflect the distinct origin and evolution of different kinds of comets. Since comets evolve into the inner solar system from distant reservoirs beyond Neptune, the flattened inclination distribution of JFCs/ECs requires a flattened source such as the Kuiper Belt and/or scattered disk (Fernández 1980; Duncan et al. 1988, LD97, Di Sisto et al. 2009, BM13). Because any association with a specific source depends on a comparison of the orbital distributions obtained in a model with observations, we first investigated how sensitive the orbital distribution of known JFCs/ECs is to different assumptions. To limit potential pollution from HTCs/NICs, we only used the cometary orbits with $P < 20$ yr and $2 < T_J < 3$ in our tests.

We found that the orbital distribution of JFCs/ECs is reasonably well-defined. To demonstrate that, we tested various ranges of H_T and plotted orbital distributions for several subsets of JFCs/ECs. The main idea behind these tests is that brighter comets are more easily detected, and their orbital distribution should therefore be less affected by observational biases. We found that the distributions of semimajor axis, inclination, and Tisserand parameter are nearly independent of any H_T cut. The biggest dependence on H_T is seen in the distribution of

⁷ As a side note, we point out that there are only very few orbits with $2\sqrt{2}q < T_J < 2$ and $q < 2$ au in Figure 1(b). This is because NICs evolve from $a \gg a_J$ and $e \sim 1$, and thus have $T_J < 2\sqrt{2}q$.

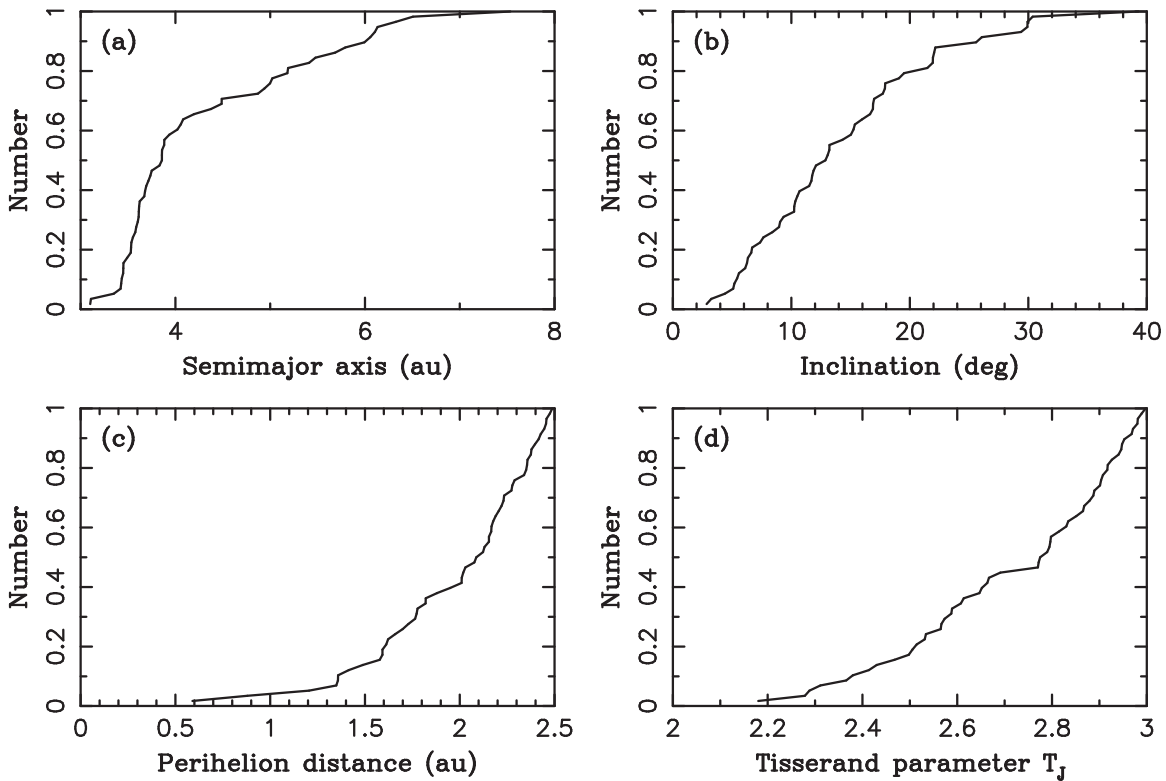


Figure 2. Cumulative orbital distributions of known JFCs/ECs with $P < 20$ yr, $2 < T_J < 3$, $q < 2.5$ au, and $H_T < 10$. All distributions shown here were normalized to 1.

perihelion distances, $q = a(1 - e)$, where limiting the sample to the brightest comets results in a distribution with slightly larger values of q . This is expected because brighter comets can be detected at larger perihelion distances.

Figure 2 shows the cumulative orbital distributions of JFCs/ECs for $P < 20$ yr, $2 < T_J < 3$, $q < 2.5$ au, and $H_T < 10$. There are 58 known comets that satisfy these criteria. Increasing the H_T cutoff results in better statistics (for example, there are 115 known JFCs/ECs with $H_T < 12$) but the perihelion distribution starts to shift toward smaller values. We therefore opted to use the 58 known JFCs/ECs with $H_T < 10$ as a base for our model comparisons in Section 4.⁸

A similar analysis was performed for HTC/NICs, where the observational biases are expected to be more severe, mainly because HTC/NICs have longer orbital periods and larger inclinations, both of which act to make their detection more difficult. To minimize the potential pollution of the sample from JFCs/ECs, we selected cometary orbits with $20 < P < 200$ yr and $T_J < 2$. There were several surprises. First, the number of known HTC/NICs increased substantially from the previous analyses of data in Levison et al. (2001, 2006). This is contributed by new detections from several ongoing near-Earth object (NEO) surveys. Second, the HTC/NIC population with $20 < P < 200$ yr and $T_J < 2$ shows a very nearly isotropic distribution of inclinations with a median inclination near 80° .

The orbital distribution of HTC/NICs with $P > 20$ yr and $T_J < 2$ is shown in Figure 3. Two sets are shown: a broader one with $a < 100$ au and $q < 4$ au (Set 1; 108 known comets), and

a narrower one with $P < 200$ yr and $q < 2$ au (Set 2; 48 known comets). This is done to highlight several things. First of all, in panel (b) of Figure 3, the inclination distribution of both sets is indeed nearly isotropic (Wang & Brasser 2014) with the median inclination $\simeq 90^\circ$ for Set 1 and $\simeq 80^\circ$ for Set 2. In contrast, using the cometary catalog available back in 2001 and criteria similar to our Set 2, Levison et al. (2001) found a median inclination of only $\simeq 45^\circ$. This led them to consider a flattened source of HTCs such as the inner, presumably flattened part of the Oort cloud, and later, in Levison et al. (2006), the scattered disk.

The perihelion distance distribution of Set 2 (Figure 3(c)) shows a sharp transition from $q < 2$ au to $q > 2$ au, indicating that the population of known comets is strongly incomplete for $q > 2$ au (ECs do not show a similar sharp transition at $q \simeq 2$ au). In fact, roughly 80% of known comets with $P > 20$ yr and $a < 100$ au have $q < 2$ au, and only $\simeq 20\%$ have $2 < q < 4$ au. This is probably related to the dependence of cometary activity on q , with comets reaching $q < 2$ au becoming active and readily detectable. To limit the influence of unknown observational biases when comparing our model with observations in Section 4, we will only consider HTC/NICs with $q < 2$ au.

Another important observational bias that must strongly affect the semimajor axis distribution in Figure 3(a) is the period dependence of comet detectability. This bias arises because comets with very long orbital periods spend most of their time at large heliocentric distances, where they show little or no activity and are not detected. This may explain the bulging profile in Figure 3(a), where roughly 40% of known comets have $a < 20$ au, while this percentage should presumably be much smaller in the underlying distribution, if the incompleteness of the known sample for long orbital periods were accounted for. To limit the effects of the orbital period

⁸ Alternatively, to limit the effects of the perihelion distance bias, we could have adopted a cut of $q < 1.5$ au (e.g., Di Sisto et al. 2009), where the distributions are (nearly) independent of H_T . We find this unnecessary with the new data and prefer to use a broader range of q .

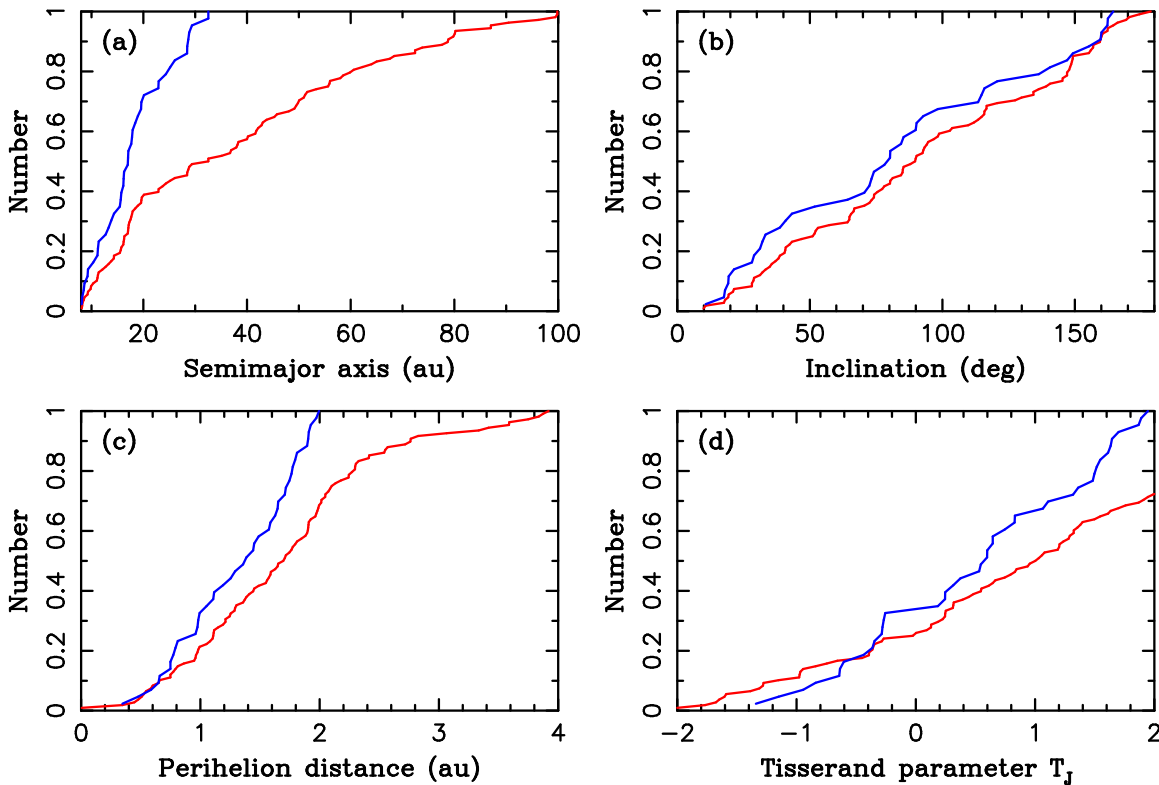


Figure 3. Cumulative orbital distributions of known comets with $P > 20$ yr, $a < 100$ au, $q < 4$ au, and $T_J < 2$ (red), and HTC/NICs with $20 < P < 200$ yr, $q < 2$ au, and $T_J < 2$ (blue).

bias, we only consider HTC/NICs with $a < 20$ au ($P < 89.4$ yr) in Section 4.

In summary, when comparing our model with observations in Section 4, we adopt the following ranges: $q < 2.5$ au, $2 < T_J < 3$, $P < 20$ yr, and $H_T < 10$ for JFCs/ECs, and $q < 2$ au, $T_J < 2$, and $20 < P < 89.4$ yr for HTC/NICs. For the reasons explained above, we believe that this sample is best suited for comparisons with our model, because it does not appear to contain any obvious signs of observational biases (that does not mean it is bias free). We use different ranges of perihelion distances for JFCs/ECs ($q < 2.5$ au) and HTC/NICs ($q < 2$ au) because these are the widest ranges of q that we can use without running into immediate problems with observational biases. In Section 4.5, where we discuss the joint model for JFCs/ECs and HTC/NICs, we use $q < 2$ au for both cometary populations.

3. Numerical Model of SPCs

In our previous work (NM12), we developed a numerical model of the early evolution of the solar system. The NM12 model follows Neptune’s migration into a massive planetesimal disk ($M_{\text{disk}} \simeq 15\text{--}20$ Earth masses, M_{\oplus}) between ~ 22 and 30 au. As the disk is dispersed during planetary migration, planetesimals are ejected from the solar system, impact planets, or end up in long-lived reservoirs such as the asteroid belt (Levison et al. 2009; Vokrouhlický et al. 2016), Jupiter Trojans (Morbidelli et al. 2005; Nesvorný et al. 2013), irregular satellites (Nesvorný et al. 2007, 2014), Kuiper Belt (Malhotra 1993; Gomes 2003; Hahn & Malhotra 2005; Levison et al. 2008; Dawson & Murray-Clay 2012; Nesvorný 2015a, 2015b; NV16), scattered disk (BM13, Kaib & Sheppard 2016; Nesvorný et al. 2016), and Oort cloud (Brasser et al. 2006, 2007, 2008; Levison

et al. 2010; Kaib et al. 2011, BM13). The NM12 model explains various properties of small-body reservoirs in the solar system. Here we use the NM12 model, in its parametrization described in NV16, to study the origin of comets.

3.1. Integration Method

Our numerical integrations consist of tracking the orbits of the four giant planets (Jupiter to Neptune) and a large number of small bodies representing the outer planetesimal disk. The terrestrial planets are not included. To set up an integration, Jupiter and Saturn are placed on their current orbits. Uranus and Neptune are placed inside their current orbits and are migrated outward. The initial semimajor axis $a_{N,0}$, eccentricity $e_{N,0}$, and inclination $i_{N,0}$ define Neptune’s orbit before the main stage of migration/instability. Here we use $a_{N,0} = 22$ au, $e_{N,0} = 0$, and $i_{N,0} = 0$.

The `swift_rmvs4` code, part of the Swift N -body integration package (Levison & Duncan 1994), is used to follow the orbital evolution of all bodies. The code was modified to include artificial forces that mimic the radial migration and damping of planetary orbits. These forces are parametrized by the exponential e -folding timescales, τ_a , τ_e , and τ_i , where τ_a controls the radial migration rate, and τ_e and τ_i control the damping rates of e and i (NV16). We set $\tau_a = \tau_e = \tau_i$ because such roughly comparable timescales were found in NM12.

The numerical integration is divided into two stages with migration/damping timescales τ_1 and τ_2 (NV16). The first migration stage is stopped when Neptune reaches $a_{N,1} \simeq 27.7$ au. Then, to approximate the effect of planetary encounters during the dynamical instability in NM12, we apply a discontinuous change of Neptune’s semimajor axis and eccentricity, Δa_N and Δe_N . Motivated by the results of NM12 and Nesvorný (2015b), we set $\Delta a_N = 0.5$ au and $\Delta e_N = 0.1$. The second

migration stage starts with Neptune having the semimajor axis $a_{N,2} = a_{N,1} + \Delta a_N$. We use the `swift_rmvs4` code and migrate the semimajor axis (and damp the eccentricity) on an e -folding timescale τ_2 . The migration amplitude was adjusted such that the planetary orbits obtained at the end of the simulations were nearly identical to the real orbits.⁹

We found from NM12 that the orbital behavior of Neptune during the first and second migration stages can be approximated by $\tau_1 \simeq 10$ Myr and $\tau_2 \simeq 30$ Myr for a disk mass $M_{\text{disk}} = 20 M_{\oplus}$, and $\tau_1 \simeq 30$ Myr and $\tau_2 \simeq 50$ Myr for $M_{\text{disk}} = 15 M_{\oplus}$. The real migration slows down, relative to a simple exponential, at late stages. Here we therefore set $\tau_1 = 10$ –30 Myr and $\tau_2 = 30$ –100 Myr. All migration simulations were run to 0.5 Gyr. They were extended to 4.5 Gyr with the standard `swift_rmvs4` code (i.e., without migration/damping after 0.5 Gyr).

3.2. Migration Graininess

We developed an approximate method to represent the jitter that Neptune’s orbit experiences due to close encounters with massive planetesimals. The method has the flexibility to use any smooth migration history of Neptune as an input, include any number of massive planetesimals in the original disk, and generate a new migration history where the random element of encounters with the massive planetesimals is taken into account. This approach is useful, because we can easily control how grainy the migration is while preserving the global orbital evolution of planets from the smooth simulations. See NV16 for a detailed description of the method. Here we set the mass of massive planetesimals to be equal to that of Pluto. This choice is motivated by the fact that two Pluto-class objects are known in the Kuiper Belt today (Pluto and Eris).

The migration graininess is included in the present integrations, because NV16 showed that grainy migration of Neptune is required to get the right proportion of resonant populations in the classical belt. The migration graininess may not be important for cometary reservoirs, but we include it in the present work for completeness.

3.3. Planetesimal Disk

The planetesimal disk was divided into two parts. The part from just outside Neptune’s initial orbit ($\simeq 22$ au) to r_{edge} represents the massive inner part of the disk (NM12). We used $r_{\text{edge}} = 28$ –30 au, because our previous simulations in NM12 showed that the massive disk’s edge must be at 28–30 au for Neptune to stop at $\simeq 30$ au (Gomes et al. 2004). The estimated mass of the planetesimal disk below 30 au is $M_{\text{disk}} \simeq 15$ –20 M_{\oplus} (NM12). The massive disk has a crucial importance here, because it was the main source from which cometary reservoirs formed (Dones et al. 2015). The planetesimal disk had an outer, low-mass extension reaching from r_{edge} to at least $\simeq 45$ au. The disk extension is needed to explain why the Cold Classics (hereafter CCs) have several unique physical and orbital properties, but it should not substantially contribute elsewhere, because of the small original mass of the extension.

Specifically, Fraser et al. (2014) estimated that the current CC population at 42–47 au represents only ~ 0.0003 Earth masses. Assuming that CCs did not lose much of its original

population during planetary migration (e.g., Nesvorný 2015b found that the primordial population of CCs was reduced by a factor of ~ 2 during early stages), this shows that the surface density of solids must have dropped substantially from 30 au to 42 au. The profile of the surface density at 30–42 au is not well constrained, but given that Neptune stopped at 30 au, it is reasonable to assume that the density decreased immediately beyond 30 au. Here we therefore choose to ignore the outer extension of the disk at > 30 au. Including it would probably not change our results substantially. Presumably, the dynamics of objects starting at 30–35 au during Neptune’s migration would be similar to those starting at < 30 au. They would become scattered by Neptune (Levison et al. 2008) with a small fraction ending in the scattered disk and Oort cloud, but this contribution should presumably be minor compared to that of the inner, more massive disk. A detailed investigation of this subject is beyond the scope of the present work.

Each of our simulations included one million disk bodies distributed from outside Neptune’s initial orbit to r_{edge} . The radial profile was set such that the disk surface density $\Sigma \propto 1/r$, where r is the heliocentric distance. The initial eccentricities and initial inclinations of disk bodies in our simulations were distributed according to the Rayleigh distribution with $\sigma_e = 0.05$ and $\sigma_i = 2^\circ$, where σ is the usual scale parameter of the Rayleigh distribution (the mean of the Rayleigh distribution is equal to $\sqrt{\pi/2} \sigma$). The disk bodies were assumed to be massless, such that their gravity did not interfere with the migration/damping routines.

3.4. Effects of Other Planets

The gravitational effects of the hypothetical fifth giant planet (Nesvorný 2011; Batygin et al. 2012, NM12) on the disk planetesimals were ignored. The fifth giant planet orbit probably crossed into the trans-Neptunian reservoirs only briefly, during some $\sim 10^5$ yr, before it was ejected by Jupiter into interstellar space. It likely did not cause major perturbations of orbits in the trans-Neptunian region, although this may depend on how exactly planets evolved during the instability (Batygin et al. 2012). In any case, it is difficult to account for the fifth giant planet with the numerical scheme used here, because its orbit evolves chaotically during the instability and cannot be easily parametrized. To include the fifth planet in a simulation, the orbital histories of planets would need to be taken directly from the self-consistent simulations of planetary instability/migration (e.g., Nesvorný et al. 2013).

P9 is hypothesized, via its gravitational shepherding effects, to produce the non-uniform distribution of orbital angles of known extreme KBOs ($a > 150$ au, $q > 35$ au; Trujillo & Sheppard 2014; Batygin & Brown 2016a). Its existence could also explain the tilt of the plane of the solar system with respect to the solar equator (Bailey et al. 2016; Lai 2016; Gomes et al. 2017), and the high inclinations of large semimajor axis Centaurs (Gomes et al. 2015, Batygin & Brown 2016b). The predicted parameters of P9 are $M_9 \gtrsim 10 M_{\oplus}$, $400 \lesssim a_9 \lesssim 900$ au, $0.4 \lesssim e_9 \lesssim 0.8$, and $i_9 \lesssim 30^\circ$. In this work, we performed several simulations with P9 to investigate the influence of P9 on the dynamical structure of distant cometary reservoirs and on comet delivery. The goal was to diagnose properties of P9 from orbital characteristics of the cometary populations.

To construct an adequate model with P9, we first need to know how and when P9 reached its current orbit. We considered several possibilities (e.g., Kenyon & Bromley 2016; Li &

⁹ The migration and damping timescales of Uranus were assumed to be the same as those of Neptune. In the NM12 simulations, the orbit of Uranus was not much affected by the instability. We therefore used $\Delta a_U = 0$ and $\Delta e_U = 0.05$.

Adams 2016). It seems to us, for example, that P9 cannot be related to the hypothesized fifth giant planet (Nesvorný 2011; Batygin et al. 2012, NM12). This is especially clear if the planetary instability happened late, because in that case it is hard to imagine any plausible mechanism that could have stabilized the fifth planet on a wide orbit. Instead, we find it more plausible that P9 reached its wide orbit well before the epoch of planetary instability (i.e., before Neptune dispersed the massive planetesimal disk below 30 au; e.g., Izidoro et al. 2015). This would mean that the dynamical origin of the trans-Neptunian populations, including distant cometary reservoirs, postdates the chain of events that ended with P9 on its wide orbit. Working under this assumption, here we performed several simulations where P9 was included as a massive perturber since $t = 0$.

3.5. Galactic Tide and Stellar Encounters

We assumed that the Galaxy is axisymmetric and the Sun follows a circular orbit of radius R_0 in the Galactic midplane. The Sun's angular speed about the Galactic center is Ω_0 . Then, from Levison et al. (2001; see also Heisler & Tremaine 1986; Wiegert & Tremaine 1999), the Galactic tidal acceleration is given by

$$\mathbf{F}_{\text{tide}} = \Omega_0^2 \left[(1 - 2\delta)x\mathbf{e}_x - y\mathbf{e}_y - \left(\frac{4\pi G\rho_0}{\Omega_0^2} - 2\delta \right)z\mathbf{e}_z \right], \quad (2)$$

where $\delta = -(A + B)/(A - B)$, A and B are the Oort constants, G is the gravitational constant, and ρ_0 is the mass density in the solar neighborhood. Here, the coordinate system $(\mathbf{e}_x, \mathbf{e}_y, \mathbf{e}_z)$ was chosen such that \mathbf{e}_x points away from the Galactic center, \mathbf{e}_y points in the direction of the Galactic rotation, and \mathbf{e}_z points toward the south Galactic pole. Rotations were applied to move between $(\mathbf{e}_x, \mathbf{e}_y, \mathbf{e}_z)$ and the reference system of our integrations, which has the Z -axis pointing along the initial angular momentum vector of the planets.

Numerically, we used $\rho_0 = 0.1 M_\odot \text{pc}^{-3}$ (M_\odot is the solar mass) in most of our simulations, and tested $\rho_0 = 0.2 M_\odot \text{pc}^{-3}$ in one case as well. The Oort constants were set to be $A = 14.82 \text{ km s}^{-1} \text{ kpc}^{-1}$ and $B = -12.37 \text{ km s}^{-1} \text{ kpc}^{-1}$, giving $\delta = -0.09$. Also, $\Omega_0 = A - B = 2.78 \times 10^{-8} \text{ yr}^{-1}$.

The effect of stellar encounters was modeled in the N -body code by adding a star at the beginning of its encounter with the Sun and removing it after the encounter was over. The stars were released and removed at the heliocentric distance of 1 pc (206,000 au). We used the model of Heisler et al. (1987) to generate stellar encounters. The model accounts for 20 species of main-sequence stars and white dwarfs. The stellar mass and number density of different stellar species were computed following the procedure outlined in Heisler et al. (1987). For each species, the velocity distribution was approximated by an isotropic Maxwellian with one-dimensional variance. The number of stellar encounters below perihelion distance q therefore followed $N(< q) \propto q^2$. The dynamical effects of passing molecular clouds were ignored.

The early stages, when the Sun presumably interacted with other stars in an embedded globular cluster (Adams 2010), are not considered here. On one hand, the effect of stellar encounters during these stages may be needed to explain the detached orbits of some extreme KBOs (e.g., Sedna and VP113; Levison et al. 2004). On the other hand, cometary-size disk planetesimals have been strongly affected by aerodynamic gas drag during the early

stages (before the nebular gas was removed by photoevaporation). Instead of being ejected to large heliocentric distances, the orbits of small bodies were probably circularized by gas drag inside and outside of planetary orbits (e.g., Brasser et al. 2007). If so, these early stages would not substantially contribute to the formation of cometary reservoirs.

3.6. Summary of Our Simulations

We performed 14 simulations in total (Table 1). Two reference simulations were performed without P9, the Galactic tide, or stellar encounters. They differed in the timescale of Neptune's migration: $\tau_1 = 30 \text{ Myr}$ and $\tau_2 = 100 \text{ Myr}$ (CASE 1 or C1 for short) and $\tau_1 = 10 \text{ Myr}$ and $\tau_2 = 30 \text{ Myr}$ (CASE 2 or C2). Other simulations used the same migration parameters as C1 or C2, but also included some combination of P9, Galactic tide, and/or stellar encounters. Three simulations were performed in C1 with no P9. In one job, we used $\rho_0 = 0.1 M_\odot \text{pc}^{-3}$ (C1G1) and no stellar encounters. The remaining two jobs were done with $\rho_0 = 0.1 M_\odot \text{pc}^{-3}$ and $\rho_0 = 0.2 M_\odot \text{pc}^{-3}$, and stellar encounters (C1G1S and C1G2S, respectively).

In addition, we performed nine simulations with different masses and orbits of P9. We used $M_9 = 10, 15, 20,$ and $30 M_\oplus$; $a_9 = 500, 700,$ or 900 au ; and $i_9 = 0^\circ, 15^\circ,$ or 30° . The eccentricity of P9 was set in each case from the solar obliquity constraint (Bailey et al. 2016; Lai 2016; Gomes et al. 2017), except for one case with $i_9 = 0$, where we used $M_9 = 20 M_\oplus$, $a_9 = 700 \text{ au}$, $e_9 = 0.6$, and C1 migration parameters. None of these simulations, except one, included effects of the Galactic tide or stellar encounters. Our most complete job with C1 migration parameters included P9 with $M_9 = 15 M_\oplus$, $a_9 = 700 \text{ au}$, $e_9 = 0.6$, $i_9 = 30^\circ$, Galactic tide with $\rho_0 = 0.1 M_\odot \text{pc}^{-3}$, and stellar encounters.

The simulations were performed on NASA's Pleiades supercomputer (10 jobs in C1, one in C2) and Prague cluster Tiger (three jobs in C2). One C1 simulation over 4.5 Gyr required about 600 hr on 25 Ivy Bridge nodes (20 cores each) of Pleiades, totaling over 34 CPU-years per simulation.

3.7. Comet Production Runs

The last integration segment, between $t = 3.5 \text{ Gyr}$ and $t = 4.5 \text{ Gyr}$ ($\Delta T = 1 \text{ Gyr}$; time t is defined such that $t = 0$ at the start of our integrations about 4.5 Gyr ago and t runs forward in time to $t = 4.5 \text{ Gyr}$ at the current epoch), was performed with a code specialized for the analysis of cometary orbits. First, we used cloning to improve the statistics of orbits reaching below Saturn's orbit. This was done by monitoring the heliocentric distance, r , of each body at each time step (0.5 yr). If $r < 9 \text{ au}$ for the first time, the body was cloned 100 times producing 100 new (cloned) orbits. The cloned orbits were generated by small random perturbation of the velocity vector of the original orbit. A similar method was used in BM13.

Second, in addition to the normal output of Swift, we modified the code to output the orbital elements of comets in 100 yr intervals. The information was written in separate output files if $a < 35 \text{ au}$, corresponding to $P \lesssim 200 \text{ yr}$, and $q < 5.2 \text{ au}$. SPCs with perihelion distances beyond the orbit of Jupiter were not recorded in the file, but some statistics for them can be obtained from the standard Swift output. The orbital elements written in the output file were rotated to the reference plane defined by the instantaneous angular momentum vector of the four outer planets (Jupiter to Neptune). This

Table 1
A Summary of the Numerical Integrations Performed in this Work

	τ_1 (Myr)	τ_2 (Myr)	M_9 (M_\oplus)	a_9 (au)	e_9	i_9 ($^\circ$)	ρ_0 ($M_\odot \text{ pc}^{-3}$)	SE
C1	30	100	0	0	no
C1G1	30	100	0	0.1	no
C1G1S	30	100	0	0.1	yes
C1G2S	30	100	0	0.2	yes
C1M15	30	100	15	700	0.6	30	0	no
C1M20a	30	100	20	500	0.5	15	0	no
C1M20b	30	100	20	700	0.6	30	0	no
C1M20c	30	100	20	900	0.78	30	0	no
C1I0	30	100	20	700	0.6	0	0	no
C1ALL	30	100	15	700	0.6	30	0.1	yes
C2	10	30	0	0	no
C2M10	10	30	10	700	0.6	30	0	no
C2M20	10	30	20	700	0.6	30	0	no
C2M30	10	30	30	700	0.6	30	0	no

Note. Column SE indicates whether stellar encounters were included in each job.

is required because P9, included in some simulations, acts to tilt the angular momentum vector of the Jovian planets by several degrees over 4.5 Gyr.

Third, a detailed output was implemented for LPCs. This was done by monitoring the heliocentric distance of each body in the simulation, including clones. If a body reached $r < 5.2$ au, we recorded the body’s and planetary state vectors into a special “LPC” file. A separate output was written in the LPC file for each perihelion passage with $q < 5.2$ au. After the whole simulation was over, in a subsequent set of simulations, we used the LPC file to set up backward integrations such that we can determine the orbital elements of each comet *before* it entered into the planetary region. The orbital elements were calculated near orbital aphelion, if the aphelion distance $Q < 200$ au, or near $r = 200$ au, if $Q > 200$ au (and for hyperbolic orbits).

Nongravitational forces on comets were ignored. We used a relatively long time step, 0.5 yr, in all main integrations, which is roughly 1/20 of Jupiter’s orbital period, and verified that using a shorter time step (we tried 0.25, 0.1, and 0.05 yr) does not significantly affect the results. The simulation results were used to build a steady-state model of comets. Initially, we used the full length of the last integration segment ($\Delta T = 1$ Gyr) to obtain the best statistics. Subsequently, we also tested how the results depend on the length of the time segment used for the analysis. Using a short time segment ΔT near the current epoch should more closely reflect the present population of comets. On the other hand, the statistics become inadequate if ΔT is too short, especially for HTC and if a short physical lifetime is assumed (see the next section). We did not find any significant differences in the results and used $\Delta T = 1$ Gyr, which has the best statistics, in the rest of this work. Note that the transfer time of comets from $q < 9$ au to $q < 2.5$ au is short (~ 6 Myr) compared to $\Delta T = 1$ Gyr. Thus, not cloning bodies that reached $q < 9$ au just before $t = 3.5$ Gyr is an adequate approximation.

3.8. Physical Lifetime of Comets

The steady-state model of SPCs is compared to observations in Section 4. In addition to the distribution of orbital elements a , q , and i , we also consider the distribution of T_j . To do this comparison correctly, as pointed out in LD97, we must account for the physical lifetime of active comets (i.e., how long comets

remain active). We considered three different parametrizations of the physical lifetime:

Number of perihelion passages with $q < 2.5$ au. In our simplest parametrization of the physical lifetime, we count the number of perihelion passages with $q < 2.5$ au $N_p(2.5)$, and assume that a comet becomes inactive if $N_p(2.5)$ exceeds some threshold. The threshold is determined by orbital fits to observations.

Time spent with $r < 2.5$ au. We determine the time spent by each body with $r < 2.5$ au, $T(2.5)$, and assume that a comet becomes inactive if $T(2.5)$ exceeds some threshold. Relative to the $N_p(2.5)$ criterion, $T(2.5)$ penalizes orbits with low q and/or low a values, because bodies with these orbits spend more time below 2.5 au.

Heliocentric distance weighted effective erosion time. Comets reaching low heliocentric distances are heated by solar irradiation and are expected to erode faster than more distant comets. The nature of the relationship between the effective¹⁰ erosion rate and heliocentric distance is uncertain. Here we assume, motivated by the heliocentric distance dependence of the water ice sublimation rate (Marsden et al. 1973), that the erosion rate is proportional to r^{-2} if $r < 2.5$ au. The time spent at each r is then weighted by r^{-2} and accumulated in $T_e(2.5)$. Relative to $T(2.5)$, $T_e(2.5)$ penalizes bodies reaching low heliocentric distances.

The parametrizations described above are a compromise between complexity and realism. More complex models, such as the splitting model of Di Sisto et al. (2009), are not considered. These models may be more realistic but have more parameters and are therefore difficult to constrain. We do not use LD97’s parametrization of the physical lifetime (see also BM13), because their parametrization was developed for ECs, and is not applicable to HTCs or LPCs, which have much longer orbital periods. Two possibilities exist for a comet to become inactive: it either becomes dormant or it disrupts and disappears. We do not distinguish between these different possibilities in this work and attempt to constrain our model from observations of *active* comets.

¹⁰ Including normal cometary activity, splitting events, etc.

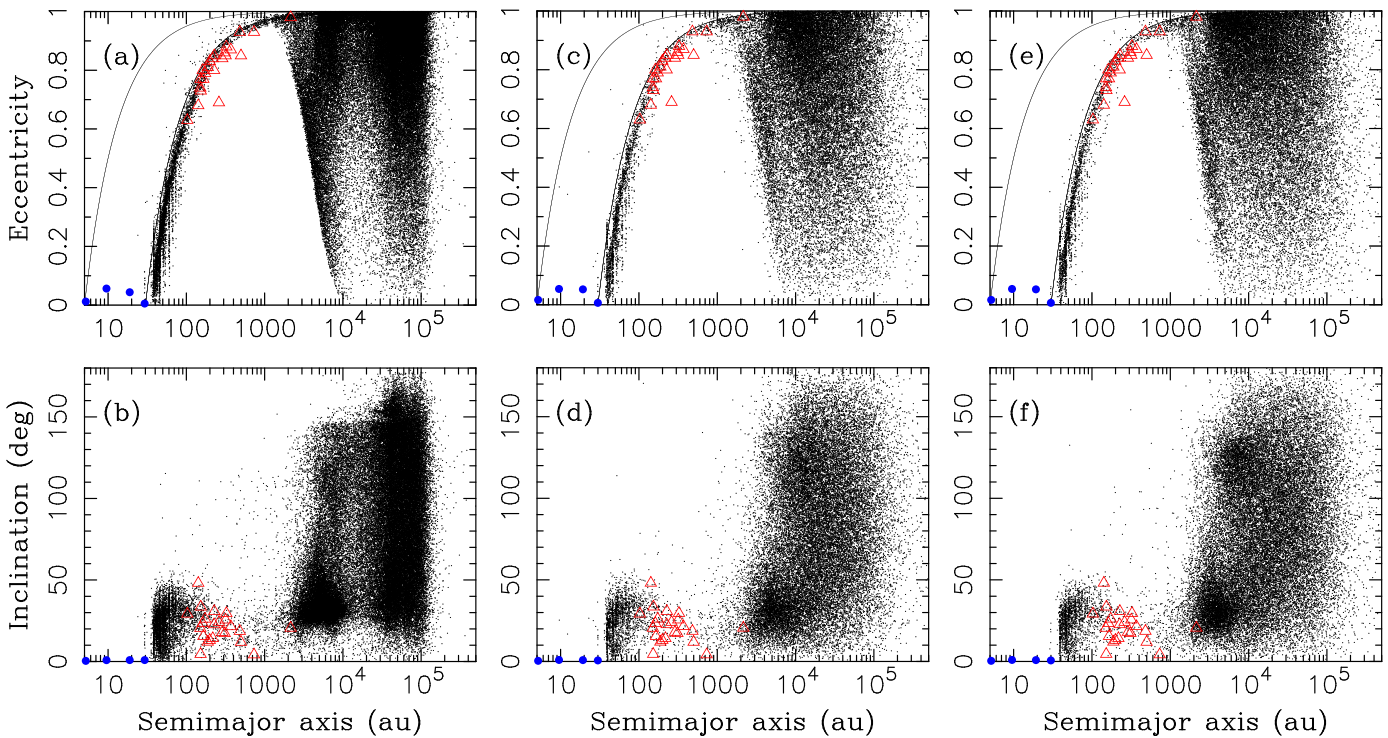


Figure 4. Orbital distribution of bodies produced in our Case 1 simulations ($\tau_1 = 30$ Myr, $\tau_2 = 100$ Myr, 4000 Plutos) at $t = 4.5$ Gyr. From left to right, the panels show results obtained in different models of external perturbations: (1) Galactic tide with $\rho_0 = 0.1 M_\odot \text{pc}^{-3}$ and no stellar encounters (C1G1; panels a and b), (2) stellar encounters and Galactic tide with $\rho_0 = 0.1 M_\odot \text{pc}^{-3}$ (C1G1S; panels c and d), and (3) stellar encounters and Galactic tide with $\rho_0 = 0.2 M_\odot \text{pc}^{-3}$ (C1G2S; panels e and f). In all cases, we subsampled the model distributions such that the orbital structures beyond 1000 au are shown with more clarity. The thin lines in the upper panels show orbits with $q = 5$ au and $q = 30$ au. Planetary orbits are denoted by blue dots. The red triangles show the orbits of known extreme KBOs. The inclination in the bottom panels is given with respect to the plane of the Jovian planets.

4. Results

4.1. Orbital Structure of the Trans-Neptunian Region

Figures 4–6 show the orbital structure of the trans-Neptunian region at the end of our simulations ($t = 4.5$ Gyr). The results of the simulations without P9 and with different assumptions about external perturbations from the Galaxy and passing stars are compared in Figure 4. There are two notable structures in Figure 4. The first one is the scattered disk that extends along the Neptune-crossing line to ~ 1000 au. The scattered disk is created when bodies encounter Neptune and are scattered along the $q \sim 30$ au line to very large heliocentric distances. The detailed orbital structure of the inner part of the scattered disk, and how it depends on Neptune’s migration, was recently discussed in Kaib & Sheppard (2016) and Nesvorný et al. (2016).

We find that the scattered disk, here defined as orbits with $50 < a < 1000$ au, contains ~ 3000 bodies at $t = 4.5$ Gyr, of which $\simeq 80\%$ have $50 < a < 200$ au (hereafter the inner SDOs). This means that the population of inner SDOs is much larger, roughly four times larger, than the population of outer SDOs ($200 < a < 1000$ au). The total number of SDOs with $50 < a < 1000$ au represents a fraction $\simeq 3 \times 10^{-3}$ of the original 10^6 disk bodies at $t = 0$, or, in terms of mass, $\simeq 0.06 M_\oplus$ for $M_{\text{disk}} = 20 M_\oplus$. This estimate is consistent with the results reported in Nesvorný et al. (2016). BM13 found from their simulations that SDOs should represent a fraction $\simeq 6 \times 10^{-3}$ of the original disk, which is a value $\simeq 2$ times larger than what we found here. The difference can be attributed to the different orbital evolutions of planets (BM13 adopted orbital histories of planets from the original Nice model and Levison et al. 2008).

In our simulations, $\simeq 1500$ bodies ended on stable orbits in the classical KB with $a < 50$ au (this includes hot classicals and resonant populations), corresponding to the fraction $\simeq 1.5 \times 10^{-3}$ of the original disk, or $\simeq 0.03 M_\oplus$. According to these results, the scattered disk should presently be ~ 2 times more populous/massive than the classical KB. For comparison, Trujillo et al. (2001) estimated from observations that the mass of the scattered disk is $\sim 0.03 M_\oplus$, which is a value two times lower than the one found here, but their 1σ uncertainty admits masses as high as $\sim 0.06 M_\oplus$, which would be in good agreement with our work. Trujillo et al. (2001) also suggested that the mass of the scattered disk is similar to that of the classical KB with $a < 50$ au, while Fraser et al. (2014) found instead that the mass of the classical KB should only be $\sim 0.01 M_\oplus$, which is three times lower than Trujillo’s estimate for the scattered disk. Thus, while there is general agreement to within a factor of a few among different works, a better characterization of the trans-Neptunian population from observations will be needed to test our model in detail.

The orbital structure of the inner scattered disk is very different from that of the outer scattered disk. Most inner SDOs ($\simeq 80\%$) are fossilized, meaning that their (barycentric) semimajor axis did not change by more than 1.5 au over the last 1 Gyr. This includes objects that interacted with Neptune’s orbital resonances in the past and subsequently decoupled from Neptune through various dynamical processes (Kaib & Sheppard 2016; Nesvorný et al. 2016). The remaining $\simeq 20\%$ of inner SDOs are being actively scattered by Neptune (hereafter the scattering SDOs; Gladman et al. 2008). Nearly all outer SDOs, on the other hand, are on scattering orbits (i.e., their semimajor axis changes by more than 1.5 au in the last 1 Gyr). Thus, even

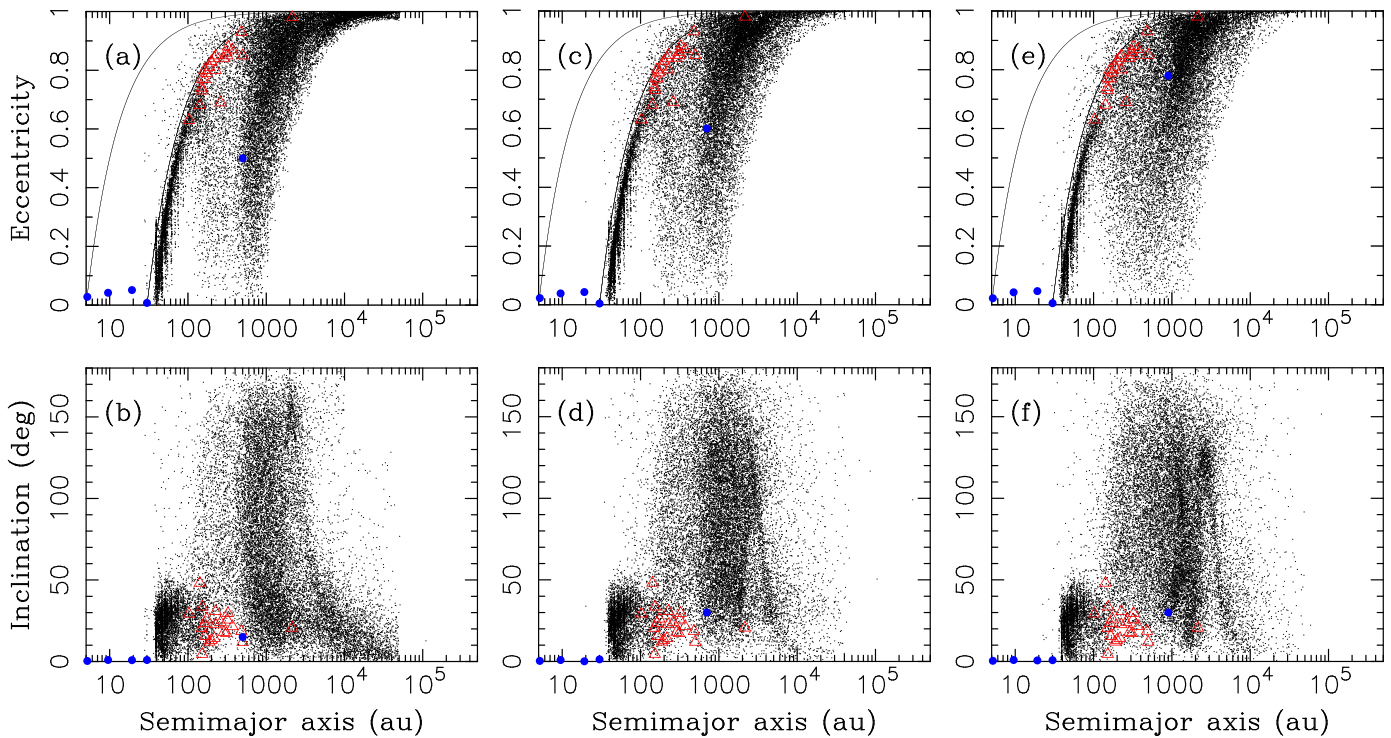


Figure 5. Orbital distribution of bodies produced in our Case 1 simulations ($\tau_1 = 30$ Myr, $\tau_2 = 100$ Myr, 4000 Plutos) at $t = 4.5$ Gyr. The Galactic tide and stellar encounters were not included here. P9 was included with the following parameters: (1) $M_9 = 20 M_\oplus$, $a_9 = 500$ au, $q_9 = 250$ au, and $i_9 = 15^\circ$ (C1M20a; panels a and b), (2) $M_9 = 20 M_\oplus$, $a_9 = 700$ au, $q_9 = 280$ au, and $i_9 = 30^\circ$ (C1M20b; panels c and d), and (3) $M_9 = 20 M_\oplus$, $a_9 = 900$ au, $q_9 = 200$ au, and $i_9 = 30^\circ$ (C1M20c; panels e and f). See Figure 4 for the meaning of the different symbols.

though the inner scattered disk is more massive than the outer one, the number of scattering objects in each population is roughly the same.

The second notable feature in Figure 4 is the Oort cloud. In Figures 4(a) and (b), where the stellar encounters were ignored, the Oort cloud has a well-defined structure with inner ($a < 20,000$ au) and outer parts ($a > 20,000$ au). The outer part of the Oort cloud forms first and is already present in our simulations in the first 10 Myr. By checking on the orbital histories of outer Oort-cloud bodies, we found that most of them reached $a > 20,000$ au after having encounters with Saturn (and typically without having encounters with Jupiter; Dones et al. 2004). In addition, a significant fraction of outer Oort-cloud bodies reached their distant orbits by being scattered by Uranus or Neptune (and without having encounters with Jupiter or Saturn). The inner Oort cloud formed as a “wave front” of orbits in our simulations that was moving from the outside in as time advanced. Most bodies that ended up in the inner Oort cloud were scattered to $a > 1000$ au by Neptune (some after having encounters with Uranus, but rarely with Jupiter/Saturn).

The gap between the inner and outer parts of the Oort cloud at $a \simeq 20,000$ au also formed gradually in our simulations as orbits were slowly removed from this region. The removal process is controlled by the period of Kozai cycles produced by the Galactic tide. For $a < 10,000$ au, the Kozai period is longer than the age of the solar system (Higuchi et al. 2007), and orbits that become decoupled from the Jovian planets by the Galactic tide do not have time to complete one Kozai cycle. These orbits persist to the end of the simulations. The orbits with $a > 10,000$ au, on the other hand, have shorter Kozai periods and can complete one or more Kozai cycles. Once the semimajor axis is above $a \sim 20,000$ au, however, the time for a comet to cycle from $q > 30$ au to $q < 30$ au to back to $q > 30$ au is substantially shorter than its

orbital period. Thus, even if q drops below 30 au, the comet may never make a passage near the planets, and the planets are thus less efficient at influencing orbits with $a > 20,000$ au.

The inner Oort cloud has an anisotropic distribution of inclinations. Two features can be noted in Figure 4(b): (1) the retrograde orbits with $a < 20,000$ au generally do not have $i > 150^\circ$, and (2) there is a concentration of prograde orbits with $i \sim 30^\circ$. Issue (1) is related to the fact that the Galactic tide below 20,000 au can be closely approximated by the quadrupole term. In the quadrupole approximation, the orbits that start with inclinations $i' < 90^\circ$ with respect to the Galactic plane cannot swap to $i' > 90^\circ$ (e.g., Naoz et al. 2013). The highest inclination that the inner Oort cloud orbits can reach with respect to the solar system plane is thus $\simeq 90^\circ + 60^\circ$, where $\simeq 60^\circ$ is the angle between the Galactic and solar system planes, or $\simeq 150^\circ$ in total. Issue (2) is also related to Kozai dynamics. The concentration for $i \sim 30^\circ$ appears because the inner Oort cloud orbits spend the most time with $i' \simeq 90^\circ$ (e.g., Higuchi et al. 2007), meaning that they are perpendicular to the Galactic plane.

The orbital features discussed above are smeared when it is accounted for stellar encounters, but they are still visible in Figures 4(c)–(f). With $\rho_0 = 0.2 M_\odot \text{ pc}^{-3}$ (simulation C1G2S; panels e and f), the inner Oort cloud extends to slightly lower semimajor axes, but its overall structure remains the same. We find that $\simeq 6.5\%$ of the original disk bodies starting at 22–30 au at $t = 0$ end up in the Oort cloud ($a > 1000$ au) at $t = 4.5$ Gyr. This is similar to the results of BM13 and somewhat higher than estimates obtained in previous dynamical models (3%–5% e.g., Dones et al. 2004; Kaib & Quinn 2008; Brassier et al. 2010; Kaib et al. 2011). With $M_{\text{disk}} = 20 M_\oplus$, we therefore find that the total mass of today’s Oort cloud should be $\sim 1.3 M_\oplus$. Of this, roughly 60% should be in the inner Oort cloud ($1000 < a < 20,000$ au) and $\simeq 40\%$ in the outer Oort cloud ($a > 20,000$ au). The

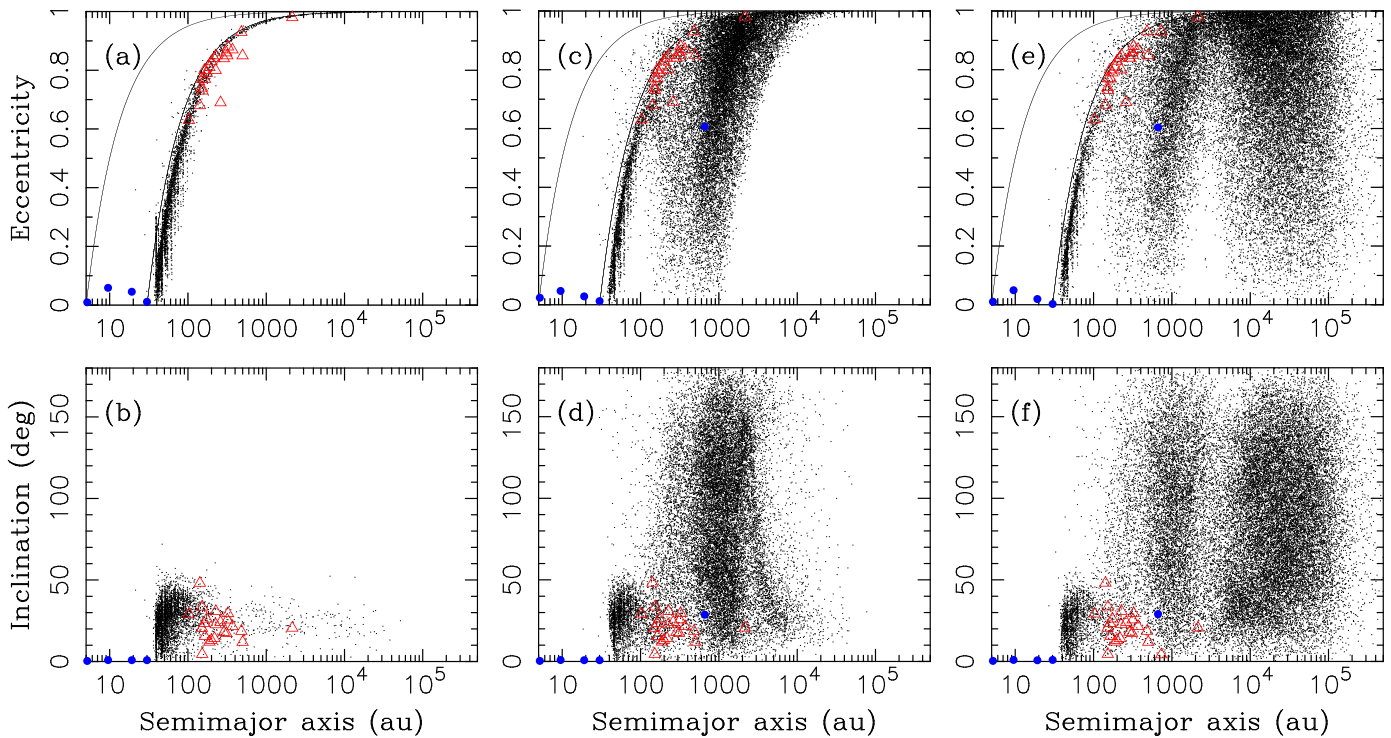


Figure 6. Orbital distribution of bodies produced in our Case 1 simulations ($\tau_1 = 30$ Myr, $\tau_2 = 100$ Myr, 4000 Plutos) at $t = 4.5$ Gyr. From left to right, the panels show results obtained in different models: (1) no P9, Galactic tide, or stellar encounters (C1; panels a and b), (2) no Galactic tide or stellar encounters, P9 with $M_9 = 15 M_\oplus$, $a_9 = 700$ au, $q_9 = 280$ au, and $i_9 = 30^\circ$ (C1M15; panels c and d), and (3) Galactic tide with $\rho_0 = 0.1 M_\odot \text{pc}^{-3}$, stellar encounters, and P9 with $M_9 = 15 M_\oplus$, $a_9 = 700$ au, $q_9 = 280$ au, and $i_9 = 30^\circ$ (C1ALL; panels e and f). See Figure 4 for the meaning of the different symbols.

Oort-cloud-to-scattered-disk ratio obtained in our simulations is found to be $\simeq 20$, while BM13 reported $\simeq 12$ from their simulations.

The orbital structure of the trans-Neptunian region dramatically changes when P9 is included in the model. To start with, we first discuss our P9 models without the Galactic tide or stellar encounters (Figure 5). The dynamical effects of P9, mainly the Kozai resonance, act to decouple SDOs from Neptune and produce a nearly isotropic cloud of bodies roughly centered at P9’s semimajor axis location. In the following, we call this hypothetical structure the P9 cloud.

Figure 5 shows how the orbital structure of the P9 cloud depends on the orbital parameters of P9. We find that $\simeq 1.7 \times 10^4$ bodies end up in the P9 cloud ($200 < a < 1000$ au) at $t = 4.5$ Gyr, corresponding to 1.7% of the original 10^6 disk bodies at $t = 0$, or $\simeq 0.34 M_\oplus$ for $M_{\text{disk}} = 20 M_\oplus$. If real, the P9 cloud would represent a population ~ 5 times larger than the classical KB and scattered disk below 200 au combined. The number of inner SDOs with $50 < a < 200$ au, and the number and orbital structure of the classical KB are not affected by P9.

Figure 6 summarizes the structure of the trans-Neptunian region in different models. Without any external perturbations, only the scattered disk is present (panels a and b), and the orbits of extreme SDOs, such as Sedna and 2012 VP113, are not obtained in the model. With P9 (panels c–f), the P9 cloud forms with an estimated mass of $\simeq 0.3\text{--}0.4 M_\oplus$. This would provide an explanation for the high- q orbits of Sedna and 2012 VP11. Shankman et al. (2017), however, claimed that the detection of known extreme KBOs would imply a very massive P9 cloud (tens of M_\oplus). This exceeds, by roughly two orders of magnitude, the P9-cloud masses inferred from our dynamical modeling. From the simulations with P9, we find that orbits similar to Sedna and 2012 VP11 have perihelion longitudes ϖ

concentrated near $\varpi - \varpi_9 = 180^\circ$ (Batygin & Brown 2016a). This concentration, however, is not strong enough, at least for the P9 parameters investigated here, to explain the current observations. We fail to identify any anisotropy in the distribution of nodal longitudes, Ω , and perihelion arguments, ω .

The orbital distribution obtained in the C1ALL model with P9 ($M_9 = 15 M_\oplus$), Galactic tide ($\rho_0 = 0.1 M_\odot \text{pc}^{-3}$), and stellar encounters is shown in Figures 6(e) and (f). Both the P9 and Oort clouds form in this model with an approximate division between them at $a \simeq 3000$ au. We find that the populations of the classical Kuiper Belt ($a < 50$ au), inner scattered disk ($50 < a < 200$ au), and P9 cloud ($200 < a < 3000$ au) represent fractions of 1.3×10^{-3} , 3.2×10^{-3} , and 0.017, respectively, which is very similar to the fractions reported for the other models above. The Oort cloud population ($a > 3000$ au) in C1ALL is somewhat smaller than in the models without P9, representing a fraction of 0.044 of the original disk (while we found a larger fraction of 0.060 for $a > 3000$ au in the C1G1S model). This probably means that the presence of P9 makes it somewhat more difficult for bodies to reach the Oort cloud.

4.2. Orbits of Ecliptic Comets

Using the methods described in Sections 3.7 and 3.8, we determined the orbital distribution of ECs in our models. Here we first discuss the results obtained without P9. Figure 7 shows the best result from the C1G1S model (Table 1). To limit the effect of observational biases discussed in Section 2, here we considered comets with $P < 20$ yr, $2 < T_J < 3$, $q < 2.5$ au, and $H_T < 10$. The best fit shown in Figure 7 was obtained with $N_p(2.5) = 500$ (Section 3.8). It turns out that similarly good fits can be obtained with other parametrizations of the physical lifetime described in Section 3.8 (e.g., $T(2.5) = 400$ yr or

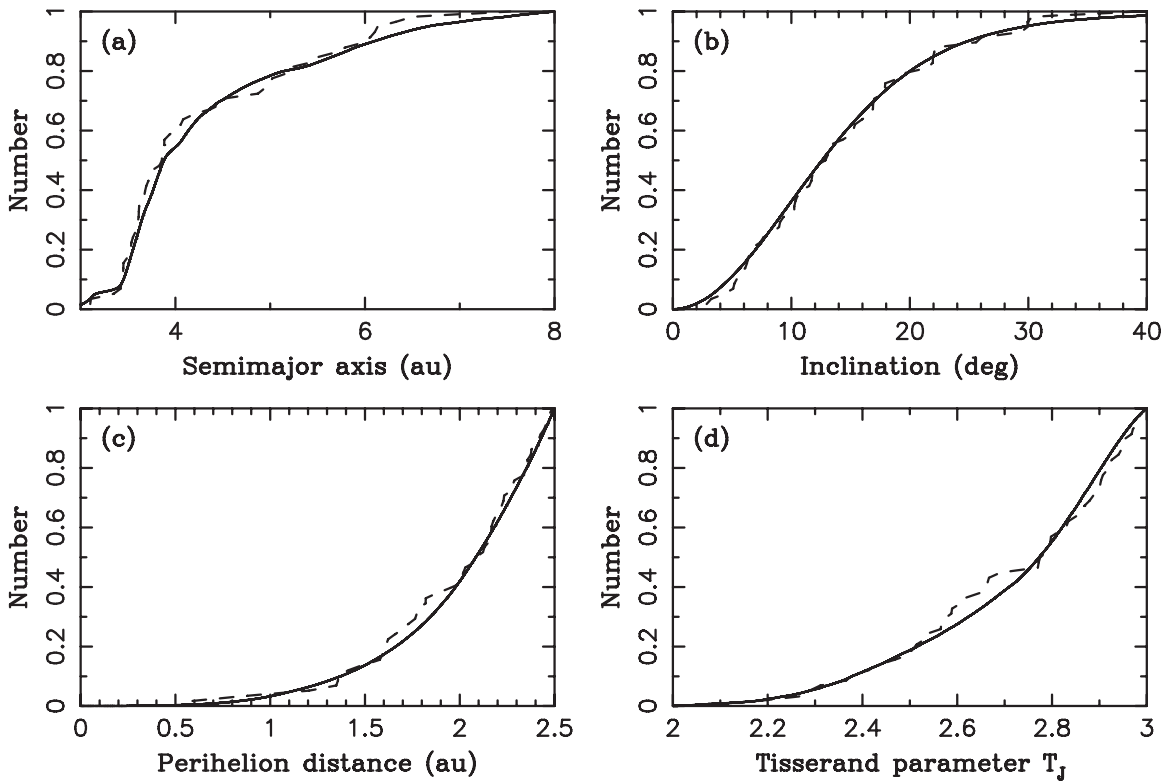


Figure 7. Cumulative orbital distributions of ECs with $P < 20$ yr, $2 < T_J < 3$, and $q < 2.5$ au. The model results from C1G1S (solid lines) are compared to the distribution of known JFCs (dashed lines; $H_T < 10$). In the model, we assumed that ECs remain active and visible for $N_p(2.5) = 500$ perihelion passages with $q < 2.5$ au.

$T_c(2.5) = 100$ yr). A realistic range of $N_p(2.5)$, as determined by the Kolmogorov–Smirnov (K–S) test, is 300–800. The models with $N_p(2.5) < 300$ or $N_p(2.5) > 800$ do not fit the observed inclination distribution of ECs. The model distributions are narrower for $N_p(2.5) < 300$ and broader for $N_p(2.5) > 800$ than the observed distribution.

The physical lifetime of comets is consistent with the results of Di Sisto et al. (2009) who found $N_p(2.5) = 300$ –450 (and $N_p(1.5) = 170$ –200). Our results are also consistent with LD97, where the physical lifetime of ECs was parametrized by the time, T_{act} , during which a comet remained active after first becoming visible (i.e., after first reaching $q < 2.5$ au). Specifically, LD97 found that $T_{\text{act}} \simeq 12,000$ yr was required to fit the inclination distribution of ECs (see also BM13). Since, according to Figure 7(a), the median orbital period of ECs is $\simeq 8$ yr, $N_p(2.5) = 500$ implies $T_{\text{act}} \simeq 4000$ yr. This is a factor of $\simeq 3$ shorter than LD97’s best estimate of T_{act} , mainly because the source of ECs in our model is the scattered disk with a wide inclination distribution (while LD97 considered the classical KB with $i < 5^\circ$). The new ECs, reaching orbits with $q < 2.5$ au for the first time, thus have a slightly wider inclination distribution in our model than in LD97. This implies shorter T_{act} .¹¹

The best-fit result shown in Figure 7 is very good. We do not need to invoke observational biases to obtain a good fit. This is satisfactory, because it leaves $N_p(2.5)$ (or, equivalently, $T(2.5)$ or $T_c(2.5)$) as the only significant free parameter that needs to be adjusted in the model. The orbital distribution of ECs is

independent of the timescale of Neptune’s migration (models C1 and C2 produce similar results) and of whether Galactic tide or stellar encounters are included in the model (models C1, C1G1, and C1G1S produce the same result). Our model is thus identified as the simplest physical/dynamical model that is capable of matching the orbital distribution of active ECs. Other, more elaborate physical models have been developed in the past (e.g., Di Sisto et al. 2009; Rickman et al. 2017), but these models have more parameters and are more difficult to constrain.

Note that our physical model must be, to some degree, unrealistic, because many known active ECs have $q > 2.5$ au. It is therefore not true that ECs can be active only when $q < 2.5$ au. When we consider ECs with $q > 2.5$ au, however, we immediately run into a problem with observational biases. First, many ECs with $q > 2.5$ au are probably undetected, even if they become active, because they appear too faint for a terrestrial observer. Second, only a fraction of ECs probably become active when reaching, say, $2.5 < q < 5$ au. Accounting for the observational incompleteness is tricky, and we do not feel confident that expanding the model in this direction would produce meaningful results. Still, for the sake of argument, we attempted to match the observed distribution of active ECs with $q < 5$ au. We found that acceptable fits can be found, for example, with $N_p(2.5) = 500$, and assuming that all comets with $q < 2.5$ au are detected, while only a fraction $(q/2.5)^{-\gamma}$ of those with $2.5 < q < 5$ au are detected, where $\gamma \sim 5$. This would indicate that only $\sim 3\%$ of ECs are detected when they reach $q \sim 5$ au, and this fraction becomes $\sim 100\%$ for $q \lesssim 2.5$ au.

Figure 8 compares the inclination distribution of ECs to those of SDOs and Centaurs. For SDOs, we used the the C1G1S simulation results at $t = 4.5$ Gyr and selected orbits with

¹¹ Rickman et al. (2017) found $T_{\text{act}} \sim 0$ from their study of JFCs, which used the simulations of Brož et al. (2013). These simulations followed the early stages of the outer planetesimal disk dispersal. They may not be adequate for the JFC population observed at the present epoch.

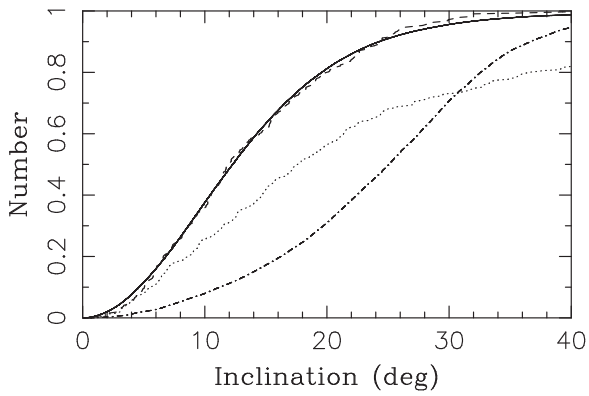


Figure 8. Inclination distribution of ECs with $P < 20$ yr, $2 < T_J < 3$, and $q < 2.5$ au. The model result (solid line; C1G1S, $N_p(2.5) = 500$) is compared to the inclination distribution of known ECs (dashed line). For reference, the plot shows the inclination distribution of model SDOs at $t = 4.5$ Gyr (dotted–dashed line) and known Centaurs (dotted line).

$50 < a < 200$ au and $q < 35$ au. This approximates the source region of ECs in our model (see Section 4.7). For Centaurs, we plotted the inclination distribution of known Centaurs from the JPL Small-Body Database Search Engine. Figure 8 shows that both the SDO and Centaur inclination distributions are significantly wider than the inclination distribution of ECs. This may seem surprising because the dynamical processes that mediate the delivery of ECs from the scattered disk, mainly the scattering encounters with planets, should act to increase the orbital inclinations and not to decrease them. By testing this, we found that the handover of bodies from the Neptune-crossing orbits toward Jupiter favors orbits with the Tisserand parameter with respect to Neptune, T_N , somewhat smaller, but not much smaller, than 3. This naturally selects the low-inclination orbits (see discussion in LD97). In addition, $2 < T_J < 3$, used here to define ECs, also favors the low-inclination orbits. Both these effects therefore contribute to create an unfamiliar situation, where the inclination distribution of the target population (ECs) is narrower than that of the source (SDOs).

4.3. EC Orbits with P9

Figure 9 shows the orbital distribution of ECs obtained in the model with P9. This is the best result that we were able to obtain with P9 in the C1M15 simulation. Other simulations with P9 produced similar results. The fit is not as good as the one in Figure 7, because in this case the inclination distribution of model ECs is somewhat broader than the inclination distribution of real ECs.¹² We applied the K–S test to understand how significant the difference is. Because, as we explained in Section 2, the inclination distribution of known ECs is not sensitive to the H_T cutoff, here we did not use any H_T cutoff to maximize the statistics. We found that the K–S probability with P9 is $p_{K-S} = 0.008$, which is to be compared to $p_{K-S} = 0.91$ obtained in the model without P9.

The difference therefore seems to be significant, indicating that ECs could be used to provide a useful constraint on P9. Related to that, we note that the difference of the inclination distributions in Figure 9 is somewhat diminished by selecting orbits with $2 < T_J < 3$. If, instead, we compare cometary

populations with $0 < T_J < 3$ (and $P < 20$ yr and $q < 2.5$ au, as usual), both the real and model inclination distributions become broader, but the discrepancy becomes more significant, because the model distribution with P9 has many high- i orbits with $P < 20$ yr. This issue cannot be resolved by considering $N_p(2.5) < 300$. This is because, with $N_p(2.5) < 300$, the model distribution with P9 has a different profile from the observed distribution (Figure 10). We found that $p_{K-S} = 6 \times 10^{-7}$ for the model with P9, $0 < T_J < 3$, and $N_p(2.5) = 100$, while $p_{K-S} = 0.89$ for the model without P9, $0 < T_J < 3$, and $N_p(2.5) = 500$. Adding to that, with $N_p(2.5) \sim 100$, there are not enough active/visible ECs in the model to explain the observed population (Section 4.6).

The problems with P9 discussed above are related to the fact that the scattering disk at $50 < a < 200$ au, which is the main source reservoir of ECs (Section 4.7), has significantly larger inclinations than in the model without P9. This happens because many SDOs interact with P9, with their orbital inclination being excited, and then return into the scattering disk with $a < 200$ au. Specifically, we find that all our simulations without P9 show similar inclination distributions of inner SDOs ($50 < a < 200$ au) with 20%–25% of scattering orbits having $i > 30^\circ$, and only 5%–7% of scattering orbits having $i > 40^\circ$. Thus, the scattering disk without P9 is relatively flat. With P9, instead, roughly 60% of scattering orbits with $50 < a < 200$ au have $i > 30^\circ$ and roughly 50% of scattering objects with $50 < a < 200$ au have $i > 40^\circ$. The scattering disk with P9 is thus apparently puffed up by the dynamical effects of P9 (see Figure 5). This is reflected by the broad inclination distribution of ECs obtained with P9.

There are several possible solutions to this problem, some of which we were able to rule out. For example, we tested P9 with zero orbital inclination with respect to the invariant plane of the solar system, and found that the inclination distribution of ECs obtained in this model (C1I0; Table 1) is practically the same as in models with $i_0 > 0$. We also verified that the same results were obtained when we used a shorter integration time step. Another possibility would be to consider P9 on an orbit with $q_0 > 300$ au, such that the effect of P9 on inner SDOs is diminished ($200 < q_0 < 300$ au in all models investigated here), and/or P9 with a lower mass. It is not clear, however, whether these cases could match other constraints such as the orbital alignment of extreme KBOs, solar obliquity, etc. A detailed investigation of this is beyond the scope of this work. Here, we found that cases with $M_9 < 15 M_\oplus$ (and $200 < q_0 < 300$ au) did not produce a sufficiently strong orbital alignment of extreme KBOs, and cases with $M_9 \gtrsim 15 M_\oplus$ produced a plausible alignment in ϖ , but not in Ω or ω .

4.4. Orbits of Halley-type Comets

Figure 11 shows the orbital distribution of HTC obtained in the C1G1S model (Galactic tide and stellar encounters included, no P9). HTCs are produced from the Oort cloud in this model. They are a low orbital period extension of the returning OCCs (e.g., Nurmi et al. 2002). The range of orbital parameters in Figure 11 is restricted to $q < 2$ au and $a < 20$ au, such that we avoid issues with the observational incompleteness of known HTCs with $q > 2$ au and/or $a > 20$ au (Section 2). In addition, here we only consider the HTC orbits with $a > 10$ au to limit the potential pollution of the sample from ECs (both HTCs and ECs are considered in the next section). While the restricted range of orbital elements is

¹² The orbital inclinations of ECs shown in Figure 7 and discussed in the following text are given with respect to the plane of the Jovian planets. A rotation to this reference plane was applied at every integration output.

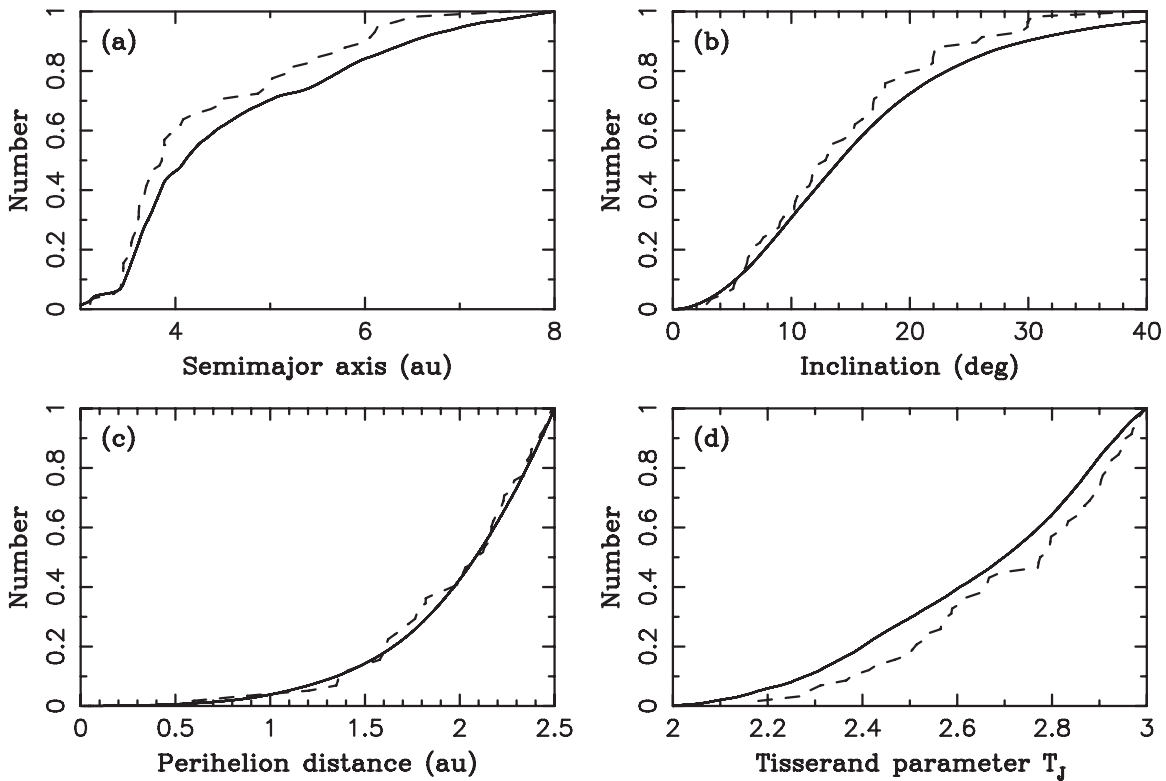


Figure 9. Same as Figure 7 but with P9 included in the simulation (C1M15; $M_9 = 15 M_\oplus$, $a_9 = 700$ au, $q_9 = 280$ au, and $i_9 = 30^\circ$).

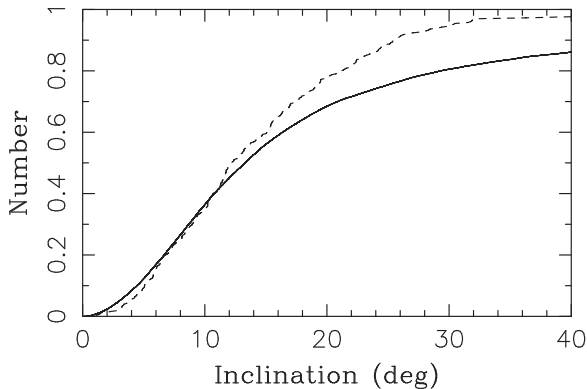


Figure 10. Same as Figure 9(b) but with $0 < T_J < 3$ and $N_p(2.5) = 100$.

probably the best-characterized part of the HTC population, the orbital distributions within this range may still be affected by observational biases. Thus, as a word of caution, we note that the comparison of model results with observations in this section is subject to some uncertainty.

With these precautions in mind, Figure 11 appears to show a relatively good agreement. HTCs produced from the Oort cloud have a nearly isotropic inclination distribution with a slight preference for prograde orbits. The model distributions of a , q , and T_J look good as well. To obtain these results, we assumed $N_p(2.5) = 3000$, which is a factor of ≈ 6 higher than what was needed to fit the inclination distribution of ECs. For HTCs, the orbital distributions are not very sensitive to $N_p(2.5)$, and $N_p(2.5) = 500$ gives qualitatively similar results to those shown in Figure 11. The value of $N_p(2.5)$ is thus not very well constrained by the fit to the observed orbital distribution of HTCs. Instead, $N_p(2.5) > 1000$ is driven by the requirement to

produce a number of active HTCs that is consistent with observations (to be discussed in Section 4.6).

We tested different parametrizations of the physical lifetime of comets described in Section 3.8 and found that they do not help solve this problem. There are several other possibilities. (1) For some reason, $N_p(2.5) \simeq 500$ derived from the fit to the inclination distribution of ECs is too low. For example, our scattered disk (in the simulations without P9) may be too excited in inclinations, which could then drive $N_p(2.5)$ to low values (because the new ECs would already have a broad inclination distribution). It is hard to imagine that this might be the case, because the scattered disk is gradually excited by encounters of SDOs with Neptune. The excitation therefore does not depend on some simulation detail. (2) The number of HTCs obtained in our model is too low, by a factor of several. This possibility is discussed in Section 5 together with our preferred resolution of this problem, where the physical lifetime of a comet is a function of the comet's size.

Figure 12 shows the orbital distributions of HTCs obtained in the C1M15 model (P9 with $M_9 = 15 M_\oplus$, and no Galactic tide or stellar encounters; Table 1). The results obtained with other parameters of P9 were similar. In this model, HTCs are produced from the P9 cloud that is roughly centered at the semimajor axis of P9 (Figure 5). The delivery of HTCs from the P9 cloud is a two-step process. First, the secular effects of P9 act to decrease the perihelion distance of an object in the P9 cloud. Subsequently, when $q < 30$ au, the orbital period of SDOs can be shortened by the gravitational effects of the Jovian planets. Since the period of secular cycles in the P9 cloud is > 100 Myr, the first step is a very slow process. This is an important difference with respect to the delivery of HTCs from the Oort cloud, where bodies can be placed on orbits with very low perihelia in one orbital period.

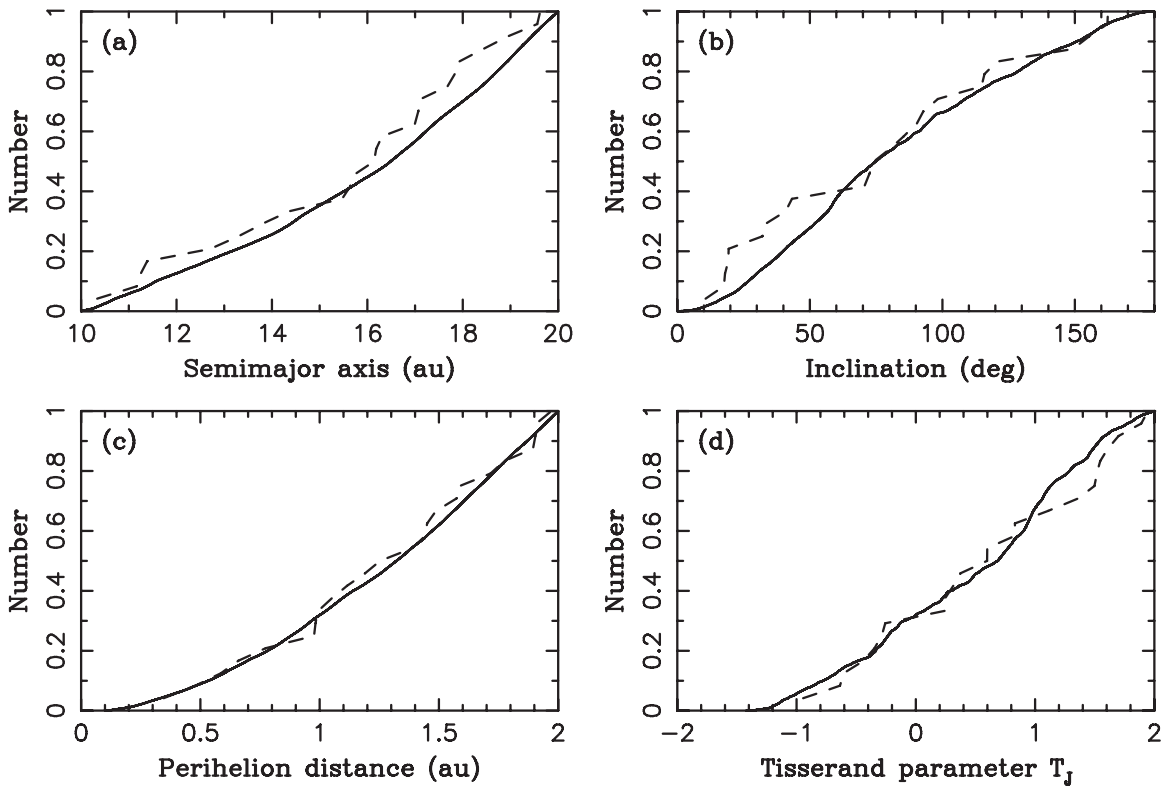


Figure 11. Cumulative orbital distributions of HTCs with $10 < a < 20$ au, $T_J < 2$ and $q < 2$ au. The model results (C1G1S; solid lines) are compared to the distribution of known HTCs (dashed lines). Here we assumed that $N_p(2.5) = 3000$.

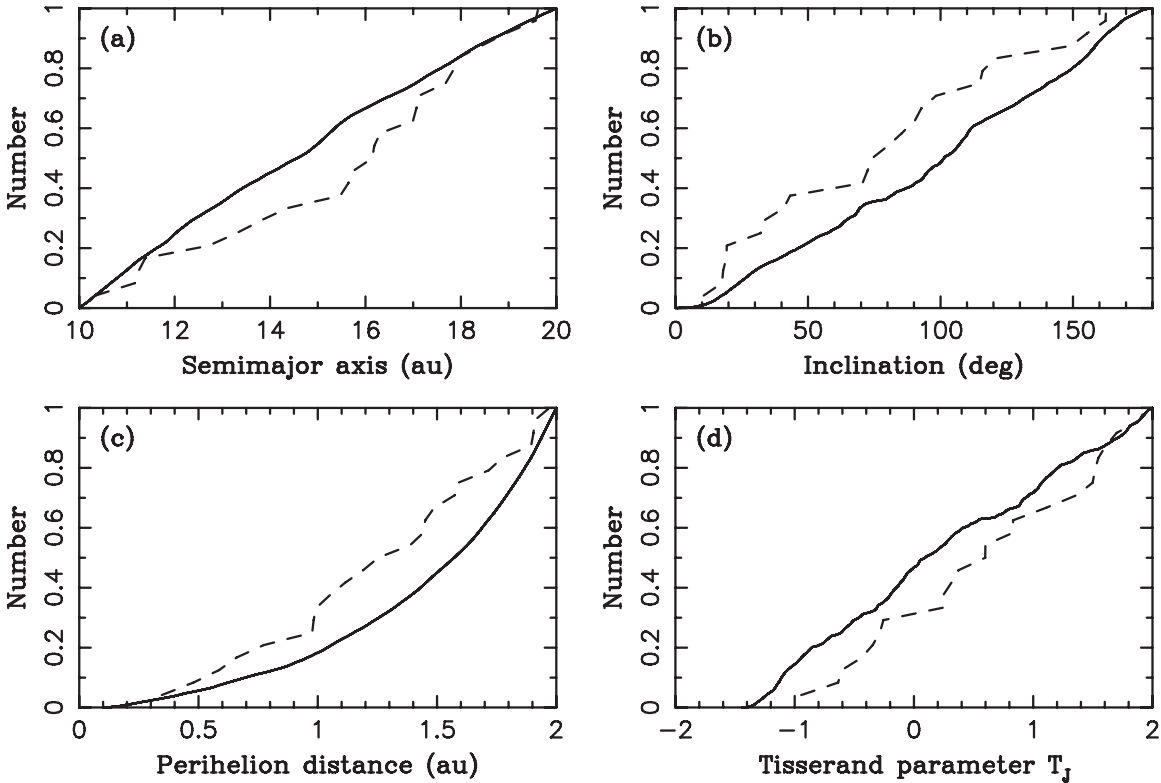


Figure 12. Same as Figure 11 but for a model with P9 (C1M15).

The HTC population obtained from the P9 cloud model shows similarities to the observed population (Figure 12), but it does not fit the orbital distribution as well as the Oort cloud model (Figure 11). The inclination distribution of model HTCs

in Figure 12(b) is very nearly isotropic with a small preference for retrograde orbits (median inclination $\simeq 100^\circ$). While this preference does not seem to be reflected in the existing observational data, it cannot be ruled out either. The perihelion

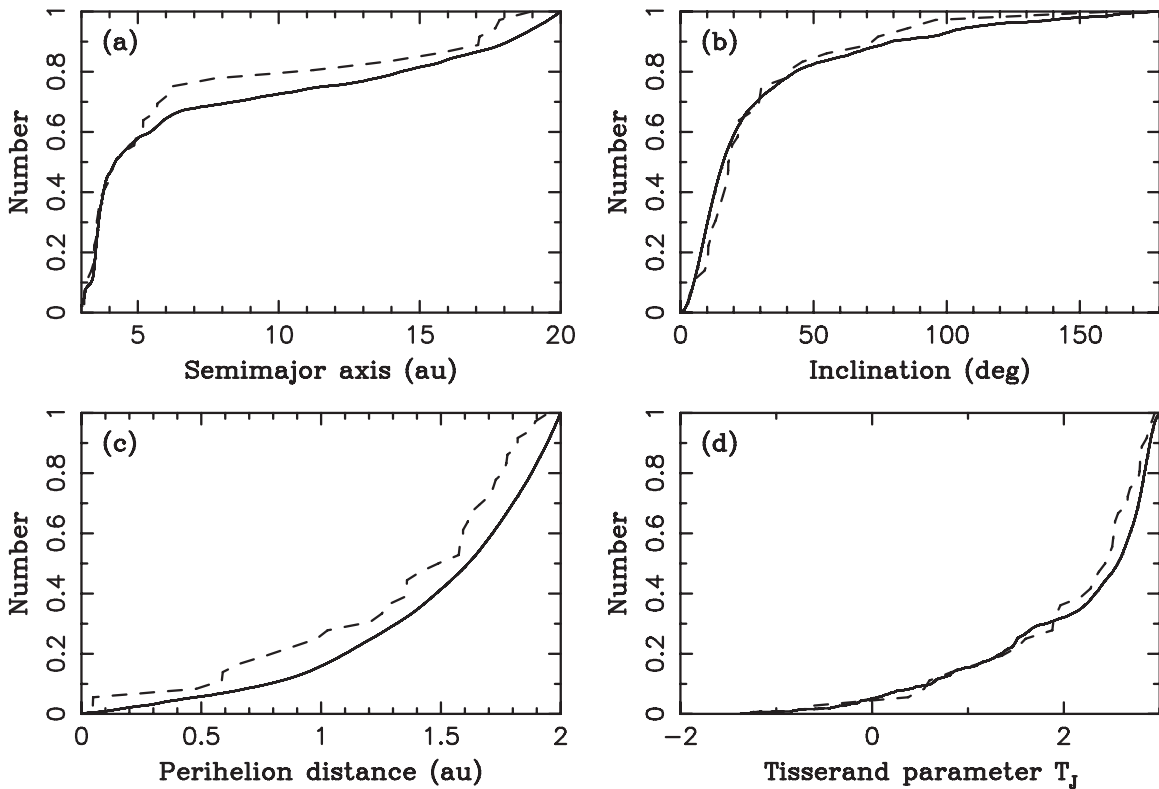


Figure 13. Cumulative orbital distributions of SPCs with $a < 20$ au, $T_J < 3$, and $q < 2$ au. The model results (solid lines; C1G1S) are compared to the distribution of known SPCs (dashed lines). In the model, we assumed that $N_p(2.5) = 500$.

distance distribution of model HTC does not fit the data too well, showing a convex profile with the number of orbits below q proportional to q^2 . The observed distribution is flatter. This may be a consequence of larger observational incompleteness for orbits with higher perihelion distances.

So far we have discussed the population of HTC with $10 < a < 20$ au and $q < 2$ au. This is because this part of orbital space should be best characterized from observations (Section 2). In a recent paper, Fernández et al. (2016) opted to use the full range $7.4 < a < 34.2$ au (corresponding to $20 < P < 200$ yr) and $q < 1.3$ au (16 known comets), and compared the orbital distribution of HTC to those obtained from LPCs and Centaurs. They argued that HTC should have had at least one perihelion passage in modern history and should thus have a good chance of being detected. They found that the distribution of orbital energy (or equivalently, of semimajor axis) obtained from LPCs does not fit the distribution of HTC. Instead, they argued that the immediate source of HTC are Centaurs. Here we confirm that HTC orbits evolving from the Oort cloud have a cumulative semimajor axis distribution $N(<a) \propto a^2$, while HTC from the P9 cloud would have a flatter distribution (that better fits the known HTC with $20 < P < 200$ yr and $q < 1.3$ au). A careful characterization of the HTC population with $a > 20$ au will be needed before these arguments can be placed on firmer ground.

In summary, we find that both the Oort and P9 clouds are potential sources of HTC, but the Oort cloud model fits the existing orbital data of HTC better than the P9 cloud model. As we will discuss in Section 4.6, the Oort cloud is a more prolific source of HTC than the P9 cloud (by a factor of ~ 2 – 3). This shows that P9 is not required from the considerations based on HTC. On the other hand, inclusion

of P9 in a model does not harm the orbital distribution of HTC.

4.5. Joint Model for ECs and HTC

Here we remove the distinction between ECs and HTC and attempt to fit the orbits of all SPCs together. Figure 13 shows the result for the C1G1S simulation (no P9) and $N_p(2.5) = 500$, which we established in Section 4.1 to be the best-fit value for ECs. The model distributions in Figure 13 have profiles similar to the observed distributions but do not fit them very well. The distribution in panel (a) can be interpreted as evidence that we have too many HTC, relative to the EC population, in our model. This would be surprising, however, because with $N_p(2.5) = 500$, the number of HTC is severely reduced (Section 4.6). If $N_p(2.5) = 3000$ instead, which is the preferred value to obtain the right number of HTC, the problem in Figure 13(a) would appear to be much worse.

We believe that this problem is related to the observational incompleteness of comets with long orbital periods. We find that the semimajor axis distributions in Figure 13 would match when it is assumed that $\sim 70\%$ of HTC with $8 < a < 20$ au have been discovered so far (while the population of ECs is assumed to be nearly complete). Note that, however, because of the issues with N_p discussed above, the intrinsic population of HTC may in reality be larger than shown in Figure 13. If so, a larger incompleteness of HTC would need to be invoked to bring the model into agreement with observations (but see discussion in Section 5, where we argue that N_p is a function of comet size and $N_p(2.5) \sim 500$ should apply to kilometer-sized comets in general).

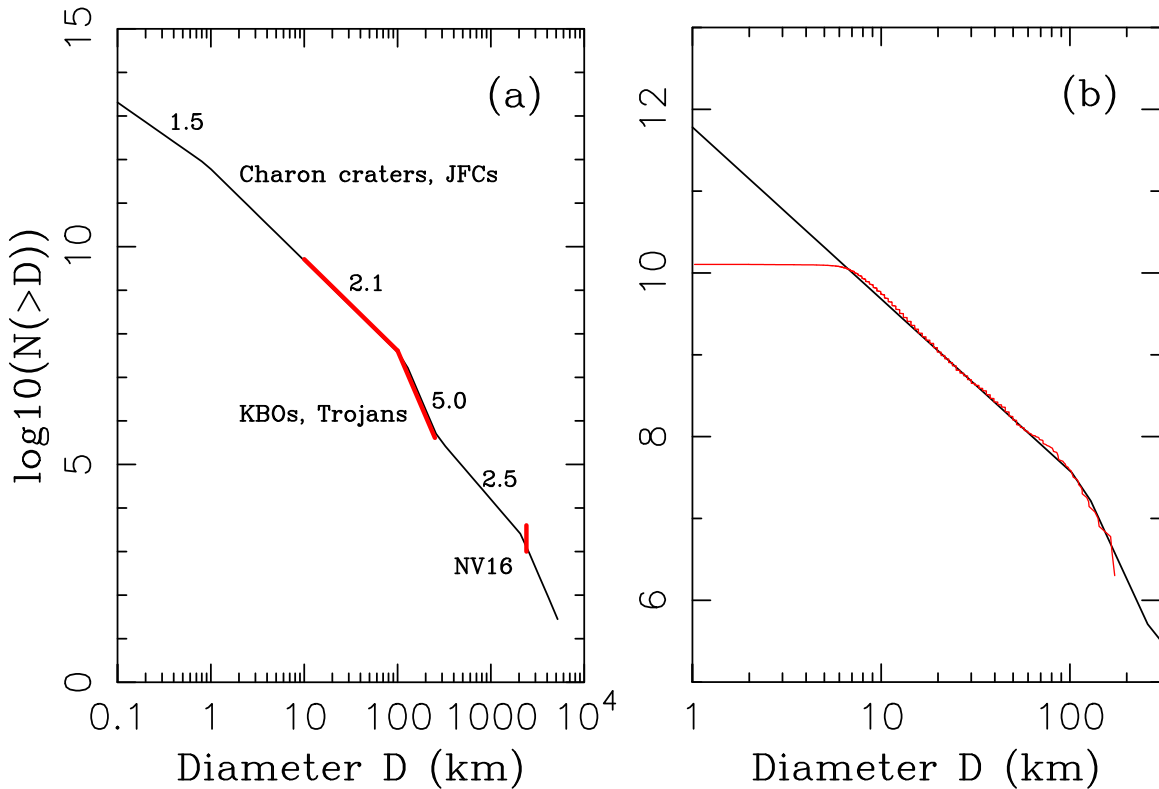


Figure 14. Size distribution of the original planetesimal disk below 30 au (panel a). The red color denotes the various constraints. The distribution for $10 < D < 300$ km was inferred from observations of Jupiter Trojans and KBOs. Panel (b) zooms in on the distribution of $1 < D < 250$ km planetesimals. The red line in panel (b) shows the size distribution of known Jupiter Trojans (the sample is incomplete for $D < 10$ km). The break between a shallow slope for small sizes and a steep slope for large sizes was fixed at $D = 100$ km. The existence of 1000–4000 Plutos in the original disk inferred in *NV16* requires that the size distribution had a hump at $D > 300$ km. The numbers above the reconstructed size distribution in panel (a) show the cumulative power index that was used for different segments. The total mass of the disk, here $M_{\text{disk}} = 20 M_{\oplus}$, is dominated by $\simeq 100$ km-class bodies.

4.6. Model Expectation for the Number of SPCs

The simulations presented here allow us to link the number of ECs and HTC to the number of planetesimals in the original trans-Neptunian disk below 30 au. This has not been done before, except by *BM13*, at least not in a self-consistent dynamical model that was also shown to reproduce many properties of other small-body populations in the solar system. In previous works, ECs and HTCs were considered separately and different schemes were developed to deal with different comet categories. In some cases, the number of ECs was linked, through a chain of multiplicative factors, to the number of objects in the present scattered disk. In other cases, the number of HTCs was calibrated by the number of observed new LPCs (e.g., *Rickman et al. 2017*). While all of these works have their own merits, here we prefer to emphasize the link to the original planetesimal disk, which presumably is the common source of ECs and HTCs. This is done as follows.

NV16 calibrated the number of bodies in the original disk. For that, they assumed that the size distribution of disk planetesimals followed the size distribution of today’s Jupiter Trojans, which is well-characterized down to at least $D \simeq 5$ km (*Wong & Brown 2015*; *Yoshida & Terai 2017*). This assumption is based on previous modeling efforts, which showed that Jupiter Trojans were implanted from the original planetesimal disk (*Morbidelli et al. 2005*; *Nesvorný et al. 2013*) and that the collisional evolution of Jupiter Trojans after their implantation was not strong enough to substantially modify their size distribution

(e.g., *Wong & Brown 2015*). To absolutely calibrate the number of original disk planetesimals, *NV16* used the estimate of the implantation probability determined in *Nesvorný et al. (2013)*, who showed that a fraction of $\simeq 7 \times 10^{-7}$ of the disk planetesimals becomes implanted on stable Trojan orbits.

The uncertainty of this estimate is not well established. In the three simulations presented in *Nesvorný et al. (2013)*, the implantation probability was found to vary by only $\simeq 15\%$. On the other hand, our new simulations with very slow planetary migration rates reveal how the survival rate of Jupiter Trojans depends on the migration timescale. Some of the results with the longest migration timescales show probabilities as low as $\simeq 3 \times 10^{-7}$. Here we therefore choose to adopt the implantation probability 5×10^{-7} , which is in the middle of the values discussed above, and use this value to calibrate the number of planetesimals in the original disk.

Additional constraints on the size distribution come from the mass of the original disk needed to generate the plausible dynamical evolution of the planetary system ($M_{\text{disk}} \simeq 20 M_{\oplus}$; *NM12*; *Deienno et al. 2017*), the expected number of Pluto-class objects in the original disk ($N_{\text{Pluto}} = 1000\text{--}4000$; *NV16*), and various Kuiper Belt constraints (see *NV16*). Figure 14 shows the reconstructed cumulative size distribution of disk planetesimals. This figure indicates that there were approximately 6×10^9 disk planetesimals with $D > 10$ km. This estimate is uncertain by a factor of ~ 2 , mainly due to the uncertainty in the implantation probability of Jupiter Trojans and its dependence on planetary migration.

The number of comets expected in a steady state, $N_{\text{com}}(>D)$, can be computed from

$$N_{\text{com}}(>D) = N_{\text{rec}} \frac{N_{\text{disk}}(>D) \Delta t}{N_{\text{sim}} \Delta T}, \quad (3)$$

where N_{rec} is the number of cometary orbits recorded in ΔT , $N_{\text{disk}}(>D)$ is the number of original disk planetesimals larger than D , $N_{\text{sim}} = 10^8$ stands for the number of bodies used in our simulations (10^6 original bodies times 100 for cloning), $\Delta t = 100$ yr is the sampling interval, and ΔT is the time interval used to accumulate good statistics. Here we use $\Delta T = 1$ Gyr ($\Delta T < 1$ Gyr leads to similar results but the statistics are worse). Note that N_{rec} depends on the assumed physical lifetime of comets.

In the following text, we compare N_{com} with the number of known comets with $D > 10$ km. There are several reasons behind this choice, perhaps the most important being that comets with small nuclei are probably more difficult to detect than those with $D > 10$ km. The known population of small comets is therefore incomplete and biased in uncertain ways. In previous work, the total absolute magnitude H_T was often taken as a proxy for the nuclear size of a comet, but we do not find any correlation when the nuclear size of the comets determined in Fernández et al. (2013) is compared to their H_T (or their nuclear magnitude) reported at the JPL site. We therefore believe that attempts to relate H_T to the nuclear size may be misguided.

We searched various catalogs to determine the number of known ECs and HTC with $D > 10$ km. There are two large ECs listed in the JPL database: 10P/Tempel 2 ($D = 10.6$ km) and 28P/Neuimin 1 ($D = 21.4$ km) (see Lamy et al. 2004 for a discussion). In addition, Fernández et al. (2013) reported four additional ECs with $D > 10$ km, two of which have $q < 2.5$ au at the present time. These are 162P/Siding Spring ($D = 14.1$ km) and 315P/LONEOS ($D = 10.8$ km).¹³ So, together, there appear to be four known ECs with $D > 10$ km and $q < 2.5$ au.

It is not known how solid this estimate is. On one hand, some size estimates were obtained from an assumed visual albedo (often taken as low as $\sim 2\%$). These determinations are less reliable than those derived from IR observations and thermal modeling. In addition, it is often assumed that the absolute nuclear magnitude can be determined from observations, either because the contribution of the coma is thought to be negligible (e.g., observations close to the orbital aphelion), or because the nucleus appears to be resolved. On the other hand, the known sample of ECs with $D > 10$ km and $q < 2.5$ au may still be incomplete. Indeed, both 162P and 315P were only discovered in 2004.

As for HTCs, there are 1P/Halley ($D = 11$ km), C/1991 L3 Levy ($D = 11.6$ km), and C/2001 OG108 LONEOS ($D = 13.6$ km). The diameter of C/1991 L3 Levy was not measured in the thermal IR and is not reliable, while the (effective) diameters of 1P/Halley and C/2001 OG108 LONEOS are well established. 109P/Swift-Tuttle with $D = 26$ km has semimajor axis $a = 26.1$ au and is outside the range considered here ($10 < a < 20$ au). We conclude that there are $\simeq 2$ – 3 known HTCs with $D > 10$ km, $q < 2$ au, and $a < 20$ au. Again, it is not clear how complete this sample is, but it should probably be

more incomplete than ECs. The large HTCs may therefore be as common as large ECs, if not even more common.

Using Equation (3), we find from our simulations without P9 that $N_{\text{EC}} = 1$ – 2 for $D > 10$ km, $2 < T_J < 3$, $P < 20$ yr, $q < 2.5$ au, and $300 < N_p(2.5) < 800$ (i.e., the range of $N_p(2.5)$ required to fit the inclination distribution; Figure 15(a) shows how N_{EC} depends on $N_p(2.5)$).¹⁴ This is somewhat lower than the number of large ECs discussed above, thus indicating that our model may be anemic, by a factor of ~ 2 – 4 , when compared to observations. This factor would be larger if the observational incompleteness of large ECs is significant. With P9 and $300 < N_p(2.5) < 800$, we obtain $N_{\text{EC}} = 0.7$ – 1 for $D > 10$ km, $2 < T_J < 3$, $P < 20$ yr, and $q < 2.5$ au. The number of ECs in a model with P9 is thus somewhat lower than in a model without P9. This is probably related to a larger excitation of the orbital inclinations of SDOs when P9 is present (see discussion in Section 4.3).

As for the HTCs, we find that the Oort cloud should produce $\simeq 2.3$ HTCs in a steady state with $D > 10$ km, $10 < a < 20$ au, $T_J < 2$, and $q < 2$ au. This is right in the middle of the range inferred from existing observations above, if the incompleteness of the existing sample could be ignored. This estimate was obtained for $N_p(2.5) = 3000$ and model C1G1S. The number of large HTCs obtained in our other Oort-cloud models is similar (2.7 in C1G1 and 1.7 in C1G2S). If $N_p(2.5) \lesssim 1000$ is assumed instead, then $N_{\text{HTC}} \lesssim 1$ (Figure 15(b)), at least $\simeq 2$ times below the value indicated by observations.

The P9 cloud is less efficient in producing HTCs than the Oort cloud. In particular, we find that $N_{\text{HTC}} = 0.9$ with $D > 10$ km, $10 < a < 20$ au, $T_J < 2$, and $q < 2$ au in the C1M15 model and $N_p(2.5) = 3000$. The population estimates obtained in other models with P9 are similar. This is a factor of $\simeq 2.5$ smaller than the number of HTCs obtained from the Oort cloud. The comparison of different models therefore shows that most HTCs should be coming from the Oort cloud, and the contribution of P9, if real, should be relatively minor. In the C1ALL model, where both P9 and the Oort cloud contribute to the population of HTCs, $N_{\text{HTC}} = 2.1$ for $N_p(2.5) = 3000$, which is very similar to the estimates obtained without P9. There are fewer HTCs coming from the Oort cloud in the C1ALL model, because the Oort cloud population is smaller (Section 4.1), but the contribution from the P9 cloud nearly compensates for the difference.

4.7. Source Reservoirs

We used our simulation results to characterize the source reservoirs of SPCs. For that, we selected ECs with $2 < T_J < 3$, $P < 20$ yr, $q < 2.5$ au, and $N_p(2.5) = 500$ and HTCs with $T_J < 2$, $10 < a < 20$ au, $q < 2$ au, and $N_p(2.5) = 3000$. The source orbits of selected ECs and HTCs in the C1G1S simulation are shown in Figure 16. For ECs, the orbits are shown at $t = 1.5$ Gyr after the start of the C1G1S simulation, or roughly 3 Gyr ago. The migration phase of Neptune has ended at this point. For HTCs, we prefer to plot their orbits at $t = 3.5$ Gyr, or roughly 1 Gyr ago. This is because the orbital structure of the Oort cloud, which is the main source reservoir of HTCs, continues to evolve over gigayears.

Most ECs ($\simeq 75\%$) were produced from the scattered disk with $50 < a < 200$ au (Figure 17). About 20% of ECs started

¹³ 172P/Yeung is not counted here because it currently has $q = 3.34$ au. 315P/LONEOS, also known as P/2004 VR9 or P/2013 V6, has $q = 2.43$ au and is just barely below the 2.5 au limit.

¹⁴ The number of ECs obtained in our models with P9 is slightly lower, $N_{\text{EC}} = 0.7$ – 0.9 .

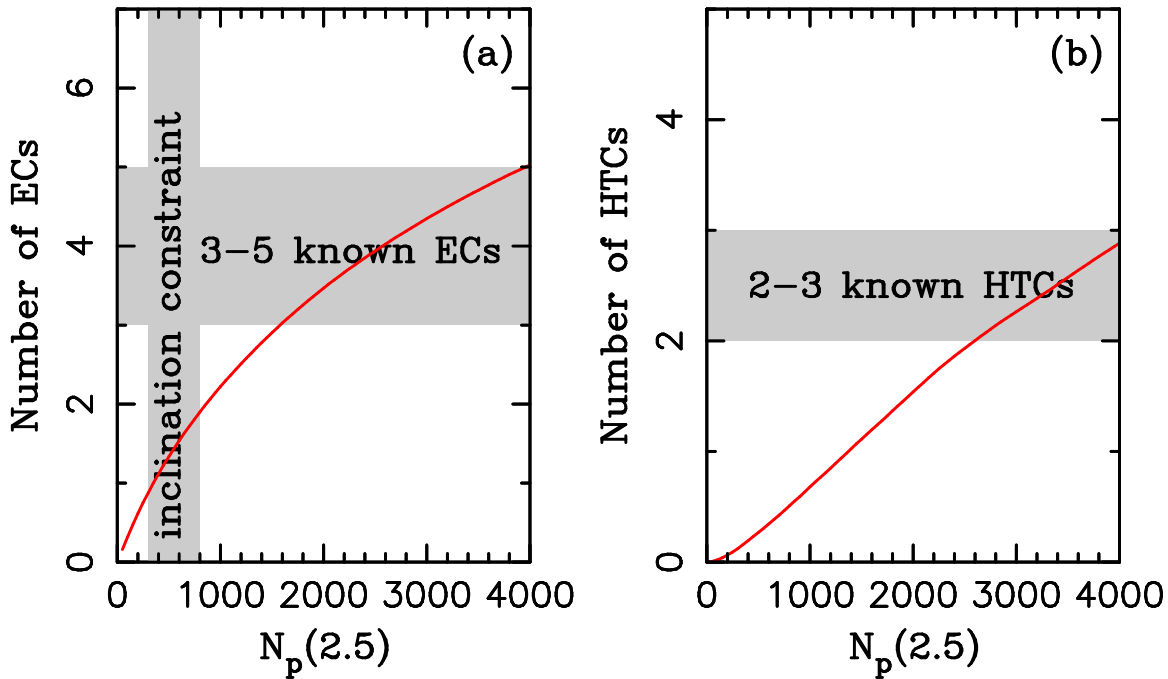


Figure 15. Number of active SPCs expected in our model. In (a), we show the expected number of active ECs with $D > 10$ km, $2 < T_J < 3$, $P < 20$ yr, and $q < 2.5$ au as a function of $N_p(2.5)$. In (b), the expected number of active HTCs with $D > 10$ km, $T_J < 2$, $10 < a < 20$ au, and $q < 2$ au is shown. These results were obtained for the C1G1S model. The horizontal shaded areas show the number of known SPCs with $D > 10$ km (and the same orbital cuts as in the model). The vertical gray strip in panel (a) is where our model fits the observed inclination distribution of ECs ($300 < N_p(2.5) < 800$). Ideally, the red line in panel (a) should run through the intersection of the two constraints.

with $a < 50$ au. Of these, most bodies had stable orbits that remained with $a < 50$ au from $t = 1.5$ Gyr to $t = 3.5$ Gyr. The classical KB, including various resonant populations below 50 au (about 4% of ECs evolved from the Plutino population in 3:2 resonance with Neptune), is therefore a relatively important source of ECs. Interestingly, $\approx 3\%$ of our model ECs started in the Oort cloud (see also Emel’yanenko et al. 2013). The orbital evolution of these comets is similar to returning LPCs or HTCs, except that they were able to reach orbits with very low orbital periods and low inclinations. The median semimajor axis of source EC orbits is ≈ 60 au. The median inclination of source EC orbits 1 Gyr ago was $\approx 20^\circ$.

Figures 16(c) and (d) show that a great majority ($\approx 95\%$) of HTCs in C1G1S come from the Oort cloud, and only $\approx 5\%$ from the $a < 100$ au region. The inclination distribution of source orbits is slightly anisotropic with the median inclination $\approx 70^\circ$ (Figure 18(c)). This is similar to the median inclination of new HTCs in our simulations. The inner and outer parts of the Oort cloud, as defined in Section 4.1 ($1000 < a < 20,000$ au inner, $a > 20,000$ au outer), contribute in nearly equal proportions to the HTC population. We see some exchange of orbits between the inner and outer Oort clouds in our simulations. The partition of source orbits therefore depends on the time when the source orbits are extracted. For example, if the orbits are extracted at $t = 0.5$ Gyr, or roughly 4 Gyr ago, then we find that $\approx 70\%$ of current-day HTCs started in the inner Oort cloud (see also Kaib & Quinn 2009).

We can now estimate the number of bodies in the source reservoirs. Because of the uncertain nature of P9, we limit the following discussion to our models without P9. Summarizing the findings discussed in the previous sections, we found that the inner SD ($50 < a < 200$ au) and Oort cloud ($a > 10,000$ au) represent the fractions $\approx 2.5 \times 10^{-3}$ and ≈ 0.065 of the original planetesimal disk. The numbers of current-day ECs and HTCs in

steady state are the fractions $\sim 2.5 \times 10^{-10}$ and $\sim 4.2 \times 10^{-10}$ of the original disk, respectively. The quoted fractions apply to active ECs ($N_p(2.5) = 500$) on orbits with $P < 20$ yr, $2 < T_J < 3$, and $q < 2.5$ au, and to active HTCs ($N_p(2.5) = 3000$) on orbits with $10 < a < 20$ au, $T_J < 2$, and $q < 2$ au. If $N_p(2.5) = 3000$ is assumed for large ECs instead (see discussion in Section 5), the fraction becomes $\sim 6.7 \times 10^{-10}$.

From these, we estimate that the ratio of active ECs with $q < 2.5$ au to inner SDOs is $\sim 2.5 \times 10^{-10} / 2.5 \times 10^{-3} = 1.0 \times 10^{-7}$ for $N_p(2.5) = 500$ or $\sim 2.7 \times 10^{-7}$ for $N_p(2.5) = 3000$. The former value is more similar to the fraction 6.7×10^{-8} obtained in BM13 for $T_{\text{act}} = 12,000$ yr. The ratio of active HTCs ($q < 2$ au, $10 < a < 20$ au) to Oort cloud bodies is $\sim 4.2 \times 10^{-10} / 0.065 = 6.5 \times 10^{-9}$ for $N_p(2.5) = 3000$. Since, as we discussed in Section 4.6, there are some four known active ECs with $D > 10$ km, there should be $\sim 4 / 1.0 \times 10^{-7} = 4.0 \times 10^7$ $D > 10$ km bodies in the inner SD if $N_p(2.5) = 500$ or $\sim 1.5 \times 10^7$ $D > 10$ km in inner SDOs if $N_p(2.5) = 3000$ (most of these have detached orbits; Section 4.1). We prefer the latter estimate for reasons that will be explained in Section 5. Also, from two to three HTCs with $D > 10$ km (Section 4.6), we estimate that the Oort cloud should contain $\sim 2.5 / 6.5 \times 10^{-9} = 3.8 \times 10^8$ $D > 10$ km comets.

According our work, the ratio of the Oort cloud to scattered disk should be OC/SD ~ 20 (Section 4.1). BM13 obtained OC/SD = 12 ± 1 from their simulations based on the original Nice model, and inferred OC/SD ~ 44 from observations. The latter estimate has a large uncertainty mainly due to the uncertain size and number of new LPCs. For example, BM13 pointed out that the flux of new LPCs may be lower than assumed before, because some LPCs thought previously to be new are actually returning LPCs (Królikowska & Dybczyński 2010). They ended

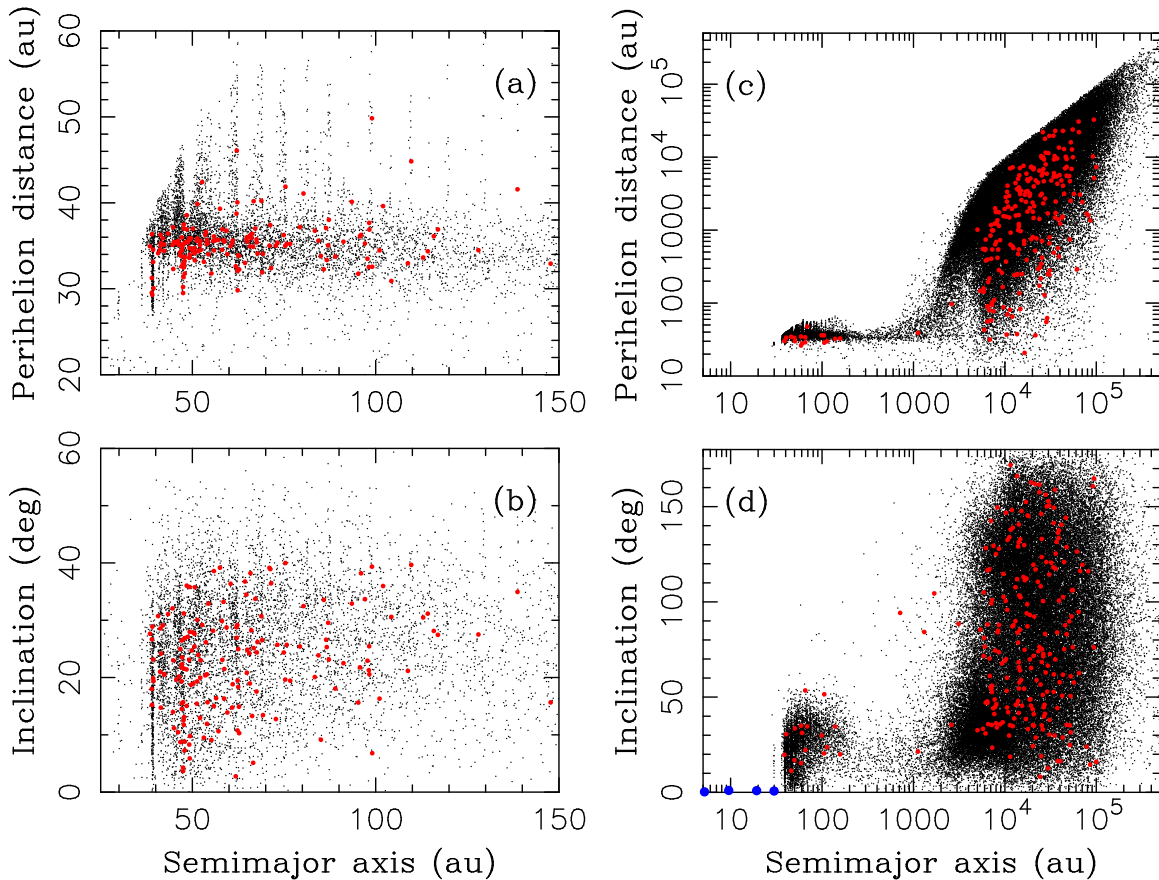


Figure 16. Orbits of trans-Neptunian bodies that dynamically evolved to become SPCs in the C1GIS model. The source of ECs is shown on the left (panels a and b). The source of HTCs is shown on the right (panels c and d). ECs were selected using $2 < T_J < 3$, $P < 20$ yr, and $q < 2.5$ au and $N_p(2.5) = 500$. We identified the source orbits of ECs at $t = 1.5$ Gyr after the start of the C1GIS integration (i.e., about 3 Gyr ago), and plotted them here with red dots. HTCs were selected using $T_J < 2$, $10 < a < 20$ au, and $q < 2$ au and $N_p(2.5) = 3000$. The source orbits of HTCs are plotted at $t = 3.5$ Gyr or about 1 Gyr ago. Background orbits are denoted by black dots.

up giving preference to OC/SD ~ 23 , roughly in the middle of the values quoted above. Our new estimate, OC/SD ~ 20 , is spot-on their preferred value.

In previous works, briefly discussed in Section 1, various estimates were given for the number of $D > 2$ km or $D > 2.3$ km bodies in the scattered disk and Oort cloud. To be able to compare with these works, we use the distribution shown in Figure 14, where the ratio of $D > 10$ km to $D > 2$ km bodies is $\simeq 29$, and the ratio of $D > 10$ km to $D > 2.3$ km bodies is $\simeq 22$. From this we find that there should be $\sim 4.4 \times 10^8$ $D > 2$ km bodies in the inner scattered disk, and $\sim 1.1 \times 10^{10}$ $D > 2$ km bodies in the Oort cloud. The former estimate is a factor of ~ 2 lower than the one reported in Rickman et al. (2017), who found, by combining several factors from LD97 and other works, that the capture rate of JFCs requires $\sim 10^9$ $D > 2$ km bodies in the scattered disk. Duncan & Levison (1997) reported $\sim 6 \times 10^8$ SDOs from their modeling of ECs (the size range to which this estimate applies was not specified), which is only slightly larger than our estimate for $D > 2$ km.

BM13 and Brassier & Wang (2015) obtained somewhat higher estimates: $\sim 2 \times 10^9$ and $\sim 6 \times 10^9$ SDOs with $D > 2.3$ km, respectively. These estimates are a factor of ~ 6 – 18 higher than ours. In addition, BM13 found that the observed flux of new LPCs implies that there are $\sim 4 \times 10^{10}$ to $\sim 10^{11}$ $D > 2.3$ km comets in the Oort cloud. These estimates are a factor of ~ 5 – 12 higher than ours. Thus, while we agree

with BM13 on the OC/SD ratio, for some reason, our best estimates are at least a factor of ~ 5 lower.

Some of the differences quoted above can be explained by the uncertain relationship between total absolute magnitude and nuclear size. As we already mentioned, we do not find any correlation when we compare H_T from the JPL database with the nuclear diameter estimates from Fernández et al. (2013). This could mean that H_T expresses comet activity rather than the nuclear size, perhaps because only a small part of a comet's surface is typically active (e.g., Sosa & Fernández 2011).

If that is the case, it may be incorrect to use H_T as a proxy for size. Brassier & Wang (2015), for example, assumed that $H_T = 10.8$ corresponds to $D = 2.3$ km and estimated that there are $\simeq 300$ JFCs with $D > 2.3$ km and $q < 2.5$ au.¹⁵ Adopting these numbers and assuming that there are ~ 4 JFCs with $D > 10$ km and $q < 2.5$ au (Section 4.6), the cumulative power-law slope at $2 < D < 10$ km would be ~ -3 , which is much steeper than the ~ -2 typically found from observations (e.g., see Lamy et al. 2004 for a review). We therefore believe that the number of small JFCs is significantly lower, possibly $\gtrsim 4$ times lower, than the one estimated in Brassier & Wang (2015).

Here we calibrated the number of large $D > 10$ km SDOs and Oort cloud bodies from Jupiter Trojans and large ECs/HTCs

¹⁵ BM13, instead, assumed that $D = 2.3$ km corresponds to $H_T = 9.3$ for JFCs and $H_T = 6.5$ for LPCs.

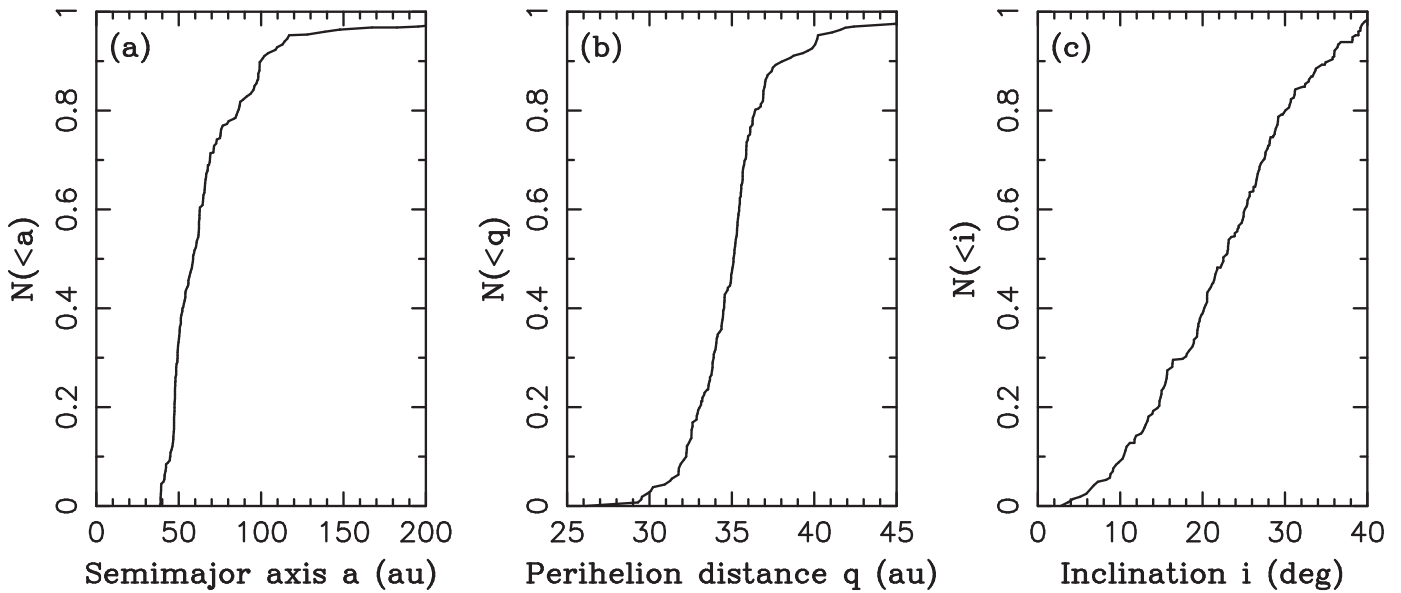


Figure 17. Orbital distribution of trans-Neptunian bodies that dynamically evolved to become ECs in our CIGIS model. The panels show the cumulative distributions of the semimajor axes (panel a), perihelion distances (panel b), and inclinations (panel c). The orbital distributions are shown for $t = 1.5$ Gyr or about 3 Gyr ago.

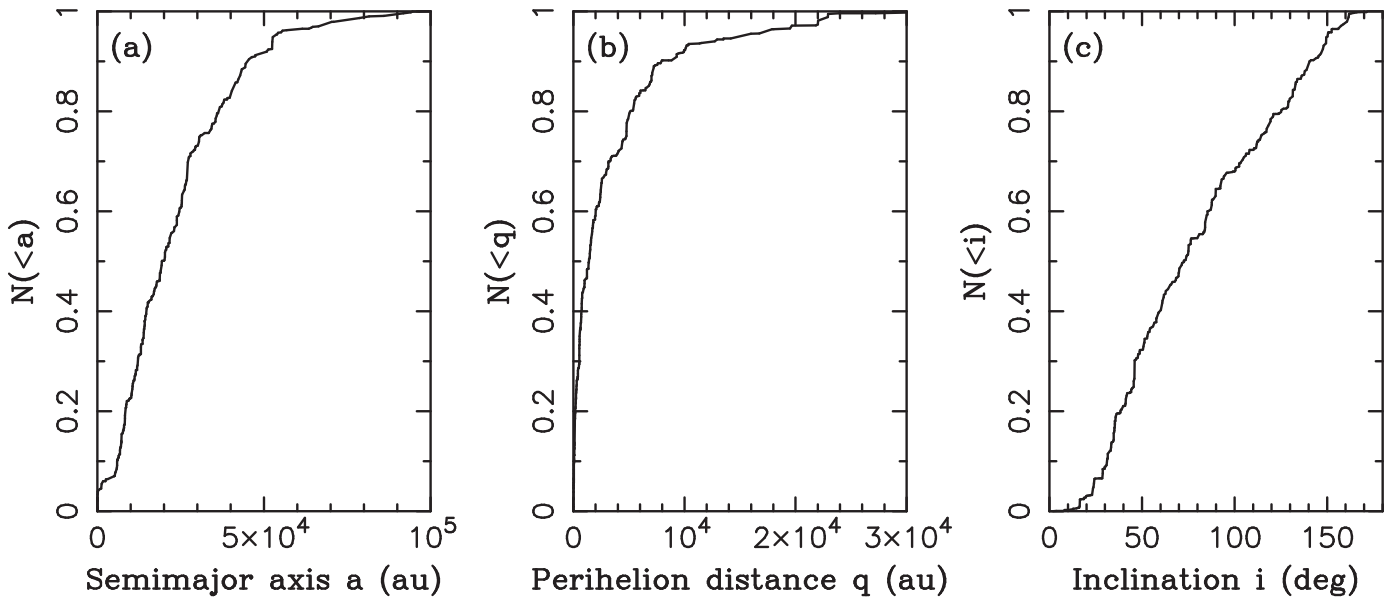


Figure 18. Orbital distribution of trans-Neptunian bodies that dynamically evolved to become HTCs in our CIGIS model. The panels show the cumulative distributions of the semimajor axes (panel a), perihelion distances (panel b), and inclinations (panel c). The orbital distributions are shown for $t = 3.5$ Gyr or about 1 Gyr ago.

for which the nuclear size is relatively well known from observations (e.g., thermal IR). These two calibrations are consistent in that they lead to the same population estimates. We then used the size distribution of Jupiter Trojans to extrapolate our estimates for $D > 10$ km to $D > 2$ km and $D > 2.3$ km. This method should provide more robust results than the previous works, because it circumvents the problems with the uncertain relationship between H_T and nuclear size.

5. Discussion

In Section 4.6, we found that our nominal model predicts ~ 2 – 4 times fewer large ECs than are required to match observations. In addition, in Sections 4.3 and 4.4, we found that

$N_p(2.5) \simeq 500$ is required to match the inclination distribution of known ECs, while $N_p(2.5) > 1000$ is required to match the number of known large HTCs. These results were obtained in a model without P9. With P9, at least for the parameters of P9 investigated here (e.g., $200 < q_0 < 300$ au), we were unable to match the inclination distribution of ECs. This problem could be potentially resolved, for example, if $q_0 > 300$ au, because in such a case P9 would presumably not excite the orbits of the inner SDO that much, resulting in a narrower inclination distribution for new ECs. It remains to be shown, however, whether P9 with $q_0 > 300$ au could be useful in explaining other data, such as the orbits of extreme KBOs and solar obliquity. A detailed investigation of this issue is beyond the scope of this work.

The discrepancy between the N_p values for ECs and HTC values is puzzling. Since both ECs and HTCs presumably formed in the same region, in the original planetesimal disk at <30 au, there is no a priori reason to think that their internal structures, and thus their physical lifetimes, should be different. Also, $N_p(2.5)$ appears to be an adequate parametrization of the physical lifetime: the results for other parametrizations, such as $T(2.5)$ or $T_c(2.5)$, are practically the same, indicating the same problem.

We believe that the low values of N_p found here for ECs cannot be a consequence of some problem with the orbital distribution of SDOs produced in our model. This is because the inclination excitation of SDOs is produced by scattering encounters with Neptune over 4.5 Gyr. The effect of these encounters should be insensitive to our setup of early Neptune’s migration and other simulation details.

Another, perhaps more plausible, solution to this problem would be if the $N_p(2.5)$ value of HTCs is shorter than found here. Since $N_p(2.5) > 1000$ of HTCs is driven by the population statistics (and not by orbital fits), better results would be obtained if the population of the Oort cloud could be increased by a factor of several. The Oort cloud population could potentially be increased, for example, if the Sun captured comets from other stars during the embedded cluster stage (Levison et al. 2010). The magnitude of this effect is, however, uncertain and a significant enhancement may require special circumstances.

Alternatively, we may have failed to properly calibrate the number of objects in the original planetesimal disk and the actual population of disk planetesimals was larger. Because the original disk was calibrated from Jupiter Trojans, this may have happened if the capture probability of stable Jupiter Trojans was significantly smaller than what we assumed in Section 4.6. It is doubtful, however, whether the calibration issue could account for the full discrepancy, because other constraints, such as the total mass of the original disk estimated in NM12, cannot be easily tweaked to produce a factor of several.

In the model developed here, the Oort cloud was populated from the planetesimal disk at $\simeq 22$ – 30 au. We did not account for the disk above 30 au, because constraints from Neptune migration (Gomes et al. 2004) and the population of CCs show that the extension of the planetesimal disk above 30 au was not very massive (relative to the disk below 30 au). The outer disk extension should thus not substantially contribute to cometary populations. We also did not account for the disk below 22 au, because the NM12 model did not account for it either. In retrospect, the contribution of the disk below 22 au to the Oort cloud needs to be reevaluated. Dones et al. (2004) showed that Jupiter-scattered planetesimals typically do not end up in the Oort cloud, because encounters with Jupiter are too powerful. Instead, the Oort cloud may have been populated from the planetesimal disk in the Saturn–Neptune zone (~ 10 – 20 au). If, for example, the surface density of planetesimals was $\Sigma \propto 1/r$, the contribution from the Saturn–Neptune zone could easily double the population of comets in the Oort cloud. It would also probably increase the number of objects in the scattered disk and bring our model to a better agreement with the number of large ECs.

Brasser et al. (2007) showed that kilometer-size comets in the Jupiter/Saturn zone cannot be ejected to the Oort cloud during the protoplanetary disk phase. This is because kilometer-size bodies immersed in a gas nebula are strongly affected by the

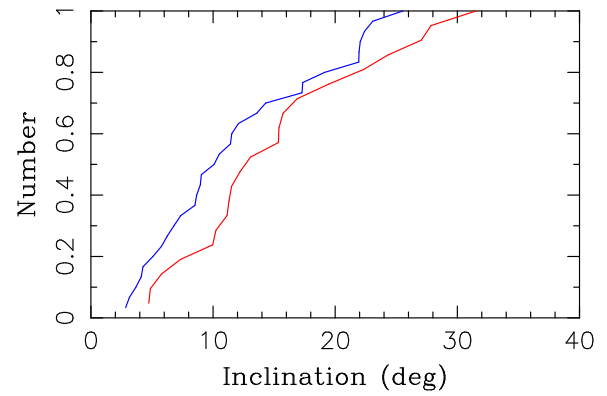


Figure 19. Inclination distribution of ECs with $q < 2.5$ au and sizes reported in Fernández et al. (2013). The red and blue lines show the distributions for large ($D > 3$ km) and small ($D < 3$ km) ECs. According to this plot, the inclination distribution of large ECs is broader than that of small ECs, as expected if the N_p value of large ECs is greater than that of small ECs.

aerodynamic drag and their orbits, instead of being ejected to large heliocentric distances, tend to circularize near (inside or outside of) planetary orbits. The Jupiter/Saturn zone should have thus been emptied of small planetesimals before the gas nebula was dispersed. The same should apply to the Uranus/Neptune zone if Uranus and Neptune formed early (e.g., Izidoro et al. 2015). If Uranus and Neptune formed relatively late (e.g., just before the nebular gas was removed), on the other hand, which may be required such that these planets did not acquire massive gas envelopes, a residual population of small planetesimals could have survived in the Uranus/Neptune zone.

The inner part of the original planetesimal disk in the Uranus/Neptune zone was not considered in previous studies, because of concerns with the delay of planetary instability, which was thought to be needed to explain the Late Heavy Bombardment (LHB) of the Moon and terrestrial planets (e.g., Gomes et al. 2005; Levison et al. 2011; Bottke et al. 2012; Marchi et al. 2012; Morbidelli et al. 2012). If asteroids were not responsible for the LHB, as argued in Nesvorný et al. (2017) and Morbidelli et al. (2017), the delay may not be needed. This motivates us to consider the planetesimal disk in the Uranus/Neptune zone. If this inner part of the disk was dispersed by planets before the main phase of Neptune’s migration, its contribution to Jupiter Trojans may have been minor, which would leave the calibration of the outer disk roughly the same.

Another important issue is the potential dependence of $N_p(2.5)$ on comet size. It is reasonable to expect that small comets should have shorter physical lifetimes than large comets. This would have interesting consequences. First, the low value of $N_p(2.5) \simeq 500$ estimated here for ECs was driven by the fit to the inclination distribution of ECs, with most contributing comets probably being ~ 1 km in size. The $D > 10$ km-class ECs, instead, could have longer physical lifetimes, which would be more consistent with the $N_p(2.5) > 1000$ estimated from the population of $D > 10$ km HTCs. If we assume, for example, that $N_p(2.5) = 3000$ for large ECs, Figure 15(a) would imply that there should be $\simeq 4.3$ $D > 10$ km ECs with $q < 2.5$ au, in excellent agreement with observations.

There are several testable consequences of this hypothesis. We used the catalog of 98 ECs from Fernández et al. (2013) and split it into two roughly equal parts corresponding to small ($D < 3$ km) and large ($D > 3$ km) comets. Figure 19 shows their inclination distributions. The expectation was, if N_p is indeed greater for larger comets, that large ECs should have a

broader inclination distribution than small ECs (because the scattering encounters with Jupiter are given more time to act with greater N_p). Figure 19 confirms this expectation. As a word of caution, we point out that the statistics in Figure 19 are relatively poor and affected by how Fernández et al. selected the sample for their *Spitzer* observations. On the other hand, we tested the dependence on the diameter cut between the small and big comets and found that the results are relatively insensitive to it. Figure 19 may thus really indicate that large comets stay active for a longer time than small comets.

BM13 argued, to explain the observed flux of new LPCs, that typical LPCs must be much smaller than typical ECs. Here we confirm this result. The flux of new LPCs is estimated from observations to be ~ 4 comets per year with $q < 5$ au and $H_T < 11$ (e.g., Francis 2005). To obtain a similar flux of new LPCs in our C1G1S simulation, we find that typical LPCs must be $D < 1$ km. In addition, in order to fit the ratio of the number of returning to new LPCs (e.g., Wiegert & Tremaine 1999), we find that $N_p(2.5) \lesssim 10$ for LPCs, nearly two orders of magnitude below the N_p values required for ECs. These results will be reported in a subsequent publication. Here we just note that some of this difference may be related to the fact that LPCs typically reach orbits with lower perihelion distances than ECs; they are thus typically exposed to stronger heating during perihelion passages and may be more active (relatively to their size) than ECs (e.g., Sosa & Fernández 2011). Together, the stronger heating and presumably smaller sizes of typical LPCs could explain why they can survive only a few perihelion passages (see also Levison et al. 2002). Large LPCs, instead, may be active much longer (hundreds to thousands of perihelion passages), with some surviving long enough to reach the short-period orbits of HTC.

The small size ($D < 1$ km) of new LPCs advocated here could appear to be in a conflict with the results of Sosa & Fernández (2011), who used measurements of the nongravitational forces to infer cometary sizes and fractions of active surface areas, f_{act} , and found that $1.3 < D < 3.6$ km for nine LPCs. This work, however, has several caveats. First, as a word of caution, we note that Sosa & Fernández assumed that the effective outflow speed of gas from a typical comet’s surface is 0.27 km s^{-1} . In reality, the effective outflow speed is unknown and depends on several parameters, including the degree of symmetry of the outflowing material. It may be possible that the LPC sizes were overestimated, for example, because the whole LPC surface is typically active, as found in Sosa & Fernández, and the outflow is more symmetrical than for SPCs. Second, only one (C/2007 W1 (Boattini)) out of nine LPCs reported in Table 3 of Sosa & Fernández (2011) had a hyperbolic orbit before entering the planetary region.¹⁶ The other LPCs in the Sosa & Fernández sample, including the giant comet C/1995 O1 (Hale-Bopp), are returning LPCs with $a < 10,000$ au. These comets survived their previous perihelion passages, and should be, consistent with our hypothesis of the dependence of the cometary survival on size, larger than typical new LPCs. A fraction of them should evolve onto HTC orbits in the future.

Figure 20 illustrates the suggested dependence of $N_p(2.5)$ on comet size. For $D > 1$ km, the profile is constrained by the fit to the inclination distribution of ECs/JFCs (for $D \sim 1$ km) and by

¹⁶ C/2007 W1 (Boattini) was estimated to have the smallest diameter ($D \simeq 1.3$ km) and is one of the two comets in the whole Sosa & Fernández sample with $f_{\text{act}} > 2$ (see that paper for the meaning of $f_{\text{act}} > 1$).

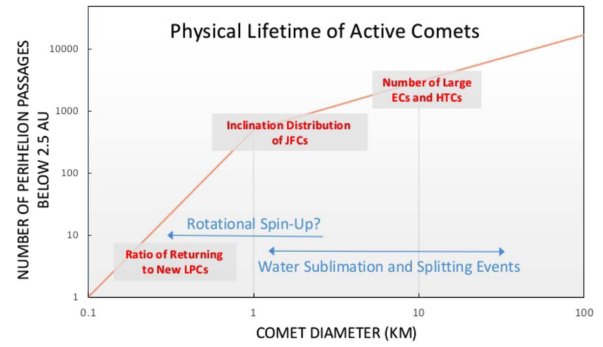


Figure 20. Schematic plot showing the suggested dependence of the physical lifetime of comets as a function of size. The physical lifetime is represented here by the number of perihelion passages below 2.5 au, $N_p(2.5)$. The red text labels constraints from which the $N_p(2.5)$ profile was obtained. As we discuss in the main text, $N_p(2.5) > 1000$ to fit the number of ECs and HTCs with $D > 10$ km. Also, $N_p(2.5) = 300\text{--}800$ to fit the inclination distribution of observed ECs, which are predominantly ~ 1 km to a few kilometers in size. The dependence of $N_p(2.5)$ on size below 1 km is uncertain. The observed ratio of returning-to-new LPCs implies that $N_p(2.5) \lesssim 10$ for the typical sizes of LPCs, which are assumed here to have $D < 1$ km. The blue text lists plausible physical mechanisms that may limit the physical lifetime of comets.

the number of large ECs and large HTCs (for $D \sim 10$ km). The dependence should be roughly linear for $D > 1$ km with $N_p(2.5) \sim 500 \times (D/1 \text{ km})$. This would be consistent with mass loss driven by surface processes (e.g., sublimation of surface ices, outbursts driven by subsurface pressure build-up). If a $D = 1$ km comet disappears on average in ~ 500 perihelion passages, the implied average erosion rate is 2 meters per perihelion passage, or $\sim 3 \times 10^9$ kg per perihelion passage for $D = 1$ km and bulk density $\rho = 500 \text{ kg m}^{-3}$. For an EC orbit, this is roughly equivalent to an average loss rate of $\sim 10 \text{ kg s}^{-1}$. For comparison, Reach et al. (2007) found the loss rate of $\sim 0.1\text{--}30 \text{ kg s}^{-1}$ from a survey of dust trails of 30 JFCs, with a median of $\sim 4 \text{ kg s}^{-1}$.

Our results are also consistent with the measured mass loss of 67P/Churyumov–Gerasimenko as determined by the *Rosetta* radio science team, $\sim 1.8 \times 10^{10}$ kg over the course of the escort phase, which may be taken as a proxy for the mass loss per orbit (Paetzold et al. 2016). If this is assumed to represent an average activity of 67P, then 67P with effective $D = 3.3$ km loses about 0.2% of its current mass per orbit. It should therefore last ~ 500 orbits at this rate. Assuming instead that the activity of 67P is driven by surface processes and will diminish as the nucleus becomes smaller, we find from the current erosion rate of ~ 1 meter per orbit that 67P will last ~ 1600 orbits. These estimates of the physical lifetime of 67P favorably compare with those given in Figure 20 for $D = 3.3$ km.

The dependence of $N_p(2.5)$ on comet size for $D < 1$ km is poorly constrained, but the physical lifetime should drop more steeply than a simple extrapolation from $D > 1$ km to $D < 1$ km would suggest (Figure 20). This is because $N_p(2.5) \lesssim 10$ to match the ratio of returning-to-new LPCs, which presumably have $D < 1$ km. We speculate that the hypothesized transition to very short physical lifetimes for comets below 1 km may be related to the rotational spin-up of small cometary nuclei and their subsequent disruption by centrifugal force (e.g., Jewitt et al.

2016). The strong dependence on size would arise in this context because the e -folding timescale of rotational spin-up is $\propto D^2$ (Jewitt 1997). Alternatively, large comets may experience periods of very low activity when the dust expelled from active areas re-accretes and creates a protective layer on the surface.

This process may not be effective for small comets because of their smaller gravity, thus implying a much shorter physical lifetime. Whatever the cause is, a dramatically shorter physical lifetime of small comets could explain the relative paucity of ECs with $D < 1$ km (e.g., Meech et al. 2004; Snodgrass et al. 2011; Fernández et al. 2013).

6. Conclusions

The main conclusions of this work are:

1. The orbital distribution of ECs is well reproduced in our models without P9. With P9, the inclination distribution of model ECs is wider than the observed one. Models with $q_0 > 300$ au could resolve this issue, but it is not clear whether they could also help match other constraints (such as the orbits of extreme KBOs and the solar obliquity).
2. We find that known HTC have a nearly isotropic inclination distribution and appear in the model as an extension of the population of returning LPCs to shorter orbital periods. The contribution to HTCs from the P9 cloud, if real, would be relatively minor.
3. The nominal model estimate of the number of large ECs falls short by a factor of $\sim 2-4$ when compared to observations. This problem can be resolved if large comets have longer physical lifetimes (see below). The number of large HTCs obtained in the model from the Oort cloud agrees well with observations.
4. We demonstrate that the physical lifetime of active comets depends on their nuclear size and explain how this can help produce the correct number of large ECs in the model. Combining the analysis of ECs, HTCs, and LPCs, we estimate that comets a few hundred meters in size should only survive several perihelion passages, ~ 1 km-class comets should be active for hundreds of perihelion passages, and ~ 10 km-class comets should live for thousands of perihelion passages. (Previously, Di Sisto et al. 2009 and Rickman et al. 2017 considered the dependence of the physical lifetime of comets on size in their models.)
5. The inner scattered disk at $50 < a < 200$ au should contain $\sim 1.5 \times 10^7$ $D > 10$ km bodies. The Oort cloud should contain $\sim 3.8 \times 10^8$ $D > 10$ km comets. These estimates can be extrapolated to smaller or larger sizes using the size distribution of Jupiter Trojans (Figure 14(b)).

The work of D.N. was supported by NASA's Emerging Worlds program. D.V. was supported by the Czech Grant Agency (grant GA13-01308S). The CPU-expensive simulations were performed on NASA's Pleiades Supercomputer and on the computer cluster Tiger at the Institute of Astronomy of Charles University, Prague. One 10^6 particle simulation over 4.5 Gyr required about 600 hr on 25 Ivy Bridge nodes (20 cores each). We greatly appreciate the support of the NASA Advanced Supercomputing Division. We thank Joel Parker for providing information about the mass loss of 67P and the anonymous reviewer for helpful suggestions to the manuscript.

References

- Adams, F. C. 2010, *ARA&A*, 48, 47
 Bailey, E., Batygin, K., & Brown, M. E. 2016, *AJ*, 152, 126
 Batygin, K., & Brown, M. E. 2016a, *AJ*, 151, 22
 Batygin, K., & Brown, M. E. 2016b, *ApJL*, 833, L3
 Batygin, K., Brown, M. E., & Betts, H. 2012, *ApJL*, 744, L3

- Botke, W. F., Vokrouhlický, D., Minton, D., et al. 2012, *Natur*, 485, 78
 Brassier, R., Duncan, M. J., & Levison, H. F. 2006, *Icar*, 184, 59
 Brassier, R., Duncan, M. J., & Levison, H. F. 2007, *Icar*, 191, 413
 Brassier, R., Duncan, M. J., & Levison, H. F. 2008, *Icar*, 196, 274
 Brassier, R., Higuchi, A., & Kaib, N. 2010, *A&A*, 516, A72
 Brassier, R., & Morbidelli, A. 2013, *Icar*, 225, 40
 Brassier, R., & Wang, J.-H. 2015, *A&A*, 573, A102
 Brož, M., Morbidelli, A., Botke, W. F., et al. 2013, *A&A*, 551, A117
 Dawson, R. L., & Murray-Clay, R. 2012, *ApJ*, 750, 43
 Deienno, R., Morbidelli, A., Gomes, R. S., & Nesvorný, D. 2017, *AJ*, 153, 153
 Di Sisto, R. P., & Brunini, A. 2007, *Icar*, 190, 224
 Di Sisto, R. P., Fernández, J. A., & Brunini, A. 2009, *Icar*, 203, 140
 Dones, L., Brassier, R., Kaib, N., & Rickman, H. 2015, *SSRv*, 197, 191
 Dones, L., Weissman, P. R., Levison, H. F., & Duncan, M. J. 2004, in *Comets II*, ed. M. C. Festou, H. U. Keller, & H. A. Weaver (Tucson, AZ: Univ. Arizona Press), 153
 Duncan, M., Quinn, T., & Tremaine, S. 1988, *ApJL*, 328, L69
 Duncan, M. J., & Levison, H. F. 1997, *Sci*, 276, 1670
 Emel'yanenko, V. V., Asher, D. J., & Bailey, M. E. 2013, *EM&P*, 110, 105
 Fernández, J. A. 1980, *MNRAS*, 192, 481
 Fernández, J. A., Gallardo, T., & Young, J. D. 2016, *MNRAS*, 461, 3075
 Fernández, Y. R., Kelley, M. S., Lamy, P. L., et al. 2013, *Icar*, 226, 1138
 Francis, P. J. 2005, *ApJ*, 635, 1348
 Fraser, W. C., Brown, M. E., Morbidelli, A., Parker, A., & Batygin, K. 2014, *ApJ*, 782, 100
 Gladman, B., Marsden, B. G., & Vanlaerhoven, C. 2008, in *The Solar System Beyond Neptune*, ed. M. A. Barucci et al. (Tucson, AZ: Univ. Arizona Press), 43
 Gomes, R., Deienno, R., & Morbidelli, A. 2017, *AJ*, 153, 27
 Gomes, R., Levison, H. F., Tsiganis, K., & Morbidelli, A. 2005, *Natur*, 435, 466
 Gomes, R. S. 2003, *Icar*, 161, 404
 Gomes, R. S., Morbidelli, A., & Levison, H. F. 2004, *Icar*, 170, 492
 Gomes, R. S., Soares, J. S., & Brassier, R. 2015, *Icar*, 258, 37
 Hahn, J. M., & Malhotra, R. 2005, *AJ*, 130, 2392
 Heisler, J., & Tremaine, S. 1986, *Icar*, 65, 13
 Heisler, J., Tremaine, S., & Alcock, C. 1987, *Icar*, 70, 269
 Higuchi, A., Kokubo, E., Kinoshita, H., & Mukai, T. 2007, *AJ*, 134, 1693
 Izidoro, A., Morbidelli, A., Raymond, S. N., Hersant, F., & Pierens, A. 2015, *A&A*, 582, A99
 Jewitt, D. 1997, *EM&P*, 79, 35
 Jewitt, D., Hsieh, H., & Agarwal, J. 2015, in *Asteroids IV*, ed. P. Michel, F. E. DeMeo, & W. F. Bottke (Tucson, AZ: Univ. Arizona Press), 221
 Jewitt, D., Mutchler, M., Weaver, H., et al. 2016, *ApJL*, 829, L8
 Kaib, N. A., & Quinn, T. 2008, *Icar*, 197, 221
 Kaib, N. A., & Quinn, T. 2009, *Sci*, 325, 1234
 Kaib, N. A., Roškar, R., & Quinn, T. 2011, *Icar*, 215, 491
 Kaib, N. A., & Sheppard, S. S. 2016, *AJ*, 152, 133
 Kenyon, S. J., & Bromley, B. C. 2016, *ApJ*, 825, 33
 Królikowska, M., & Dybczyński, P. A. 2010, *MNRAS*, 404, 1886
 Lai, D. 2016, *AJ*, 152, 215
 Lamy, P. L., Toth, I., Fernandez, Y. R., & Weaver, H. A. 2004, in *Comets II*, ed. M. C. Festou, H. U. Keller, & H. A. Weaver (Tucson, AZ: Univ. Arizona Press), 223
 Levison, H. F., Bottke, W. F., Gounelle, M., et al. 2009, *Natur*, 460, 364
 Levison, H. F., Dones, L., & Duncan, M. J. 2001, *AJ*, 121, 2253
 Levison, H. F., & Duncan, M. J. 1994, *Icar*, 108, 18
 Levison, H. F., & Duncan, M. J. 1997, *Icar*, 127, 13
 Levison, H. F., Duncan, M. J., Brassier, R., & Kaufmann, D. E. 2010, *Sci*, 329, 187
 Levison, H. F., Duncan, M. J., Dones, L., & Gladman, B. J. 2006, *Icar*, 184, 619
 Levison, H. F., Morbidelli, A., Dones, L., et al. 2002, *Sci*, 296, 2212
 Levison, H. F., Morbidelli, A., & Dones, L. 2004, *AJ*, 128, 2553
 Levison, H. F., Morbidelli, A., Tsiganis, K., Nesvorný, D., & Gomes, R. 2011, *AJ*, 142, 152
 Levison, H. F., Morbidelli, A., Van Laerhoven, C., Gomes, R., & Tsiganis, K. 2008, *Icar*, 196, 258
 Li, G., & Adams, F. C. 2016, *MNRAS*, 463, 393
 Luu, J., Marsden, B. G., Jewitt, D., et al. 1997, *Natur*, 387, 573
 Malhotra, R. 1993, *Natur*, 365, 819
 Marchi, S., Bottke, W. F., Kring, D. A., & Morbidelli, A. 2012, *E&PSL*, 325, 27
 Marsden, B. G., Sekanina, Z., & Yeomans, D. K. 1973, *AJ*, 78, 211

- Meech, K. J., Hainaut, O. R., & Marsden, B. G. 2004, *Icar*, **170**, 463
- Morbidelli, A., Levison, H. F., Tsiganis, K., & Gomes, R. 2005, *Natur*, **435**, 462
- Morbidelli, A., Marchi, S., Bottke, W. F., & Kring, D. A. 2012, *E&PSL*, **355**, 144
- Morbidelli, A., Nesvorný, D., Laurenz, V., et al. 2017, *Icar*, submitted
- Morbidelli, A., Tsiganis, K., Crida, A., Levison, H. F., & Gomes, R. 2007, *AJ*, **134**, 1790
- Naoz, S., Farr, W. M., Lithwick, Y., Rasio, F. A., & Teysandier, J. 2013, *MNRAS*, **431**, 2155
- Nesvorný, D. 2011, *ApJL*, **742**, L22
- Nesvorný, D. 2015a, *AJ*, **150**, 73
- Nesvorný, D. 2015b, *AJ*, **150**, 68
- Nesvorný, D., & Morbidelli, A. 2012, *AJ*, **144**, 117
- Nesvorný, D., Roig, F., & Bottke, W. F. 2017, *AJ*, **153**, 103
- Nesvorný, D., & Vokrouhlický, D. 2016, *ApJ*, **825**, 94
- Nesvorný, D., Vokrouhlický, D., & Deienno, R. 2014, *ApJ*, **784**, 22
- Nesvorný, D., Vokrouhlický, D., & Morbidelli, A. 2007, *AJ*, **133**, 1962
- Nesvorný, D., Vokrouhlický, D., & Morbidelli, A. 2013, *ApJ*, **768**, 45
- Nesvorný, D., Vokrouhlický, D., & Roig, F. 2016, *ApJL*, **827**, L35
- Nurmi, P., Valtonen, M. J., Zheng, J. Q., & Rickman, H. 2002, *MNRAS*, **333**, 835
- Paetzold, M., Andert, T., Hahn, M., et al. 2016, in AAS Meeting, **48**, 116.27
- Reach, W. T., Kelley, M. S., & Sykes, M. V. 2007, *Icar*, **191**, 298
- Rickman, H., Gabryszewski, R., Wajer, P., et al. 2017, *A&A*, **598**, A110
- Shankman, C., Kavelaars, J. J., Lawler, S. M., Gladman, B. J., & Bannister, M. T. 2017, *AJ*, **153**, 63
- Snodgrass, C., Fitzsimmons, A., Lowry, S. C., & Weissman, P. 2011, *MNRAS*, **414**, 458
- Sosa, A., & Fernández, J. A. 2011, *MNRAS*, **416**, 767
- Tisserand, F. 1889, *BuAsI*, **6**, 289
- Trujillo, C. A., Jewitt, D. C., & Luu, J. X. 2001, *AJ*, **122**, 457
- Trujillo, C. A., & Sheppard, S. S. 2014, *Natur*, **507**, 471
- Tsiganis, K., Gomes, R., Morbidelli, A., & Levison, H. F. 2005, *Natur*, **435**, 459
- Vokrouhlický, D., Bottke, W. F., & Nesvorný, D. 2016, *AJ*, **152**, 39
- Volk, K., & Malhotra, R. 2008, *ApJ*, **687**, 714
- Wang, J.-H., & Brasser, R. 2014, *A&A*, **563**, A122
- Wiegert, P., & Tremaine, S. 1999, *Icar*, **137**, 84
- Wong, I., & Brown, M. E. 2015, *AJ*, **150**, 174
- Yoshida, F., & Terai, T. 2017, arXiv:1706.10017